etem 830-H-15
NASI. 60:. 1182-

MAY 24 1978

NASA Technical Paper 1182

COMPLETED
ORIGINAL

Simulation Studies of Wide and Medium Field of View Earth Radiation Data Analysis

Richard N. Green

MAY 1978

NASA

48

eter 830-H-15

NAS 1.60:1182

NASA Technical Paper 1182

Simulation Studies of Wide and Medium Field of View Earth Radiation Data Analysis

Richard N. Green
Langley Research Center
Hampton, Virginia

National Aeronautics
and Space Administration

**Scientific and Technical
Information Office**

1978

SUMMARY

A parameter estimation technique is presented to estimate the radiative flux distribution over the Earth from radiometer measurements at satellite altitude. The technique analyzes measurements from a wide field of view (WFOV), horizon to horizon, nadir pointing sensor with a mathematical technique to derive the radiative flux estimates at the top of the atmosphere for resolution elements smaller than the sensor field of view. A computer simulation of the data analysis technique is presented for both Earth emitted and reflected radiation. Zonal resolutions are considered as well as the global integration of plane flux. An estimate of the equator-to-pole gradient is obtained from the zonal estimates. Sensitivity studies of the derived flux distribution to directional model errors are also presented. In addition to the WFOV results, medium field of view results are presented.

INTRODUCTION

The ability to predict climate is becoming increasingly important to the well-being of the United States and the world. The importance of the Earth's radiation budget in determining climate has long been recognized. The Earth-orbiting satellite provides a platform, outside the Earth's atmosphere, which is capable of simultaneously monitoring the outgoing reflection of the Sun's energy from the Earth's surface and atmosphere and monitoring the long-wave radiation emitted by the Earth and its atmosphere. Equally important, satellites are capable of monitoring these fluxes on a daily, monthly, or even a yearly basis. These capabilities provide the opportunity to conduct detailed studies of the variations in the radiation budget of the Earth, the effects of natural and man-made changes in the environment, and the effects which changes in the energy budget produce on the weather and climate of the Earth.

The simplicity of the wide field of view (WFOV) radiometer makes it desirable for Earth radiation mapping purposes if adequate spatial resolution can be obtained. The problem is depicted in figures 1 and 2. The WFOV radiometer receives radiation from all points on the Earth's surface from nadir to horizon. (See fig. 1.) For an orbit with an altitude of 600 km, the field of view is a circle with a diameter of 48^{o} great circle arc. The radiation leaving the atmosphere is directionally dependent and thus so is the radiation impinging on the sensor at satellite altitude. Furthermore, as seen in figure 2, this directional dependence is different at the two altitudes. The resolution which can be obtained with a set of overlapping measurements is better than that of a single measurement, as is illustrated in figure 3. For example, the location of a hot spot in an otherwise constant field can easily be determined to be within the shaded area. Recent theoretical developments (refs. 1 to 4) indicate that the spatial resolution associated with a set of WFOV measurements can be better than the instrument field of view, although the resolution obtainable does not match that obtainable by a narrow field of view scanning radiometer. Refer-

ence 4 presents a statistical filtering technique for parameter estimation which inverts WFOV satellite data to obtain estimates of the radiative fluxes at the top of the atmosphere. The technique developed requires an a priori knowledge of the directional characteristics of exiting radiation. Because a satellite measurement of flux is necessarily indirect, directional modeling is required of any technique for obtaining flux values on any scale smaller than the globe. (For example, see ref. 5.)

In this paper a data analysis technique is simulated to demonstrate its feasibility for both Earth-emitted and Earth-reflected radiation. For the purpose of this paper, Earth-emitted radiation is defined as that part of the spectrum between 5.0 and 50 μm and Earth-reflected radiation is that part of the spectrum between 0.2 and 5.0 μm. No assumption is made about the design of the sensor except the field of view, a flat-plate cosine response, and the ability to distinguish between the two wavelength bands. Mathematical models are developed to represent simulated measurement data from a WFOV radiometer onboard an orbiting satellite. The simulated measurements are then analyzed by the parameter estimation technique to yield an estimated radiation field at the top of the atmosphere. By comparing the estimated field to the "true" radiation field, the effects of directional model errors are studied.

The parameter estimation technique is also simulated for a medium field of view (MFOV) radiometer. Here the field of view does not extend from nadir to the horizon but is restricted to a smaller area. Measurements from this sensor are simulated and then analyzed to yield an estimated radiation field at the top of the atmosphere.

SYMBOLS

A	area of surface element, m^2
a	albedo
B	matrix of influence coefficients or bidirectional function
ECA	Earth central angle, deg
F	directional function for emitted radiation, sr^{-1}
f	true anomaly of satellite, deg
G	equator-to-pole gradient, W/m^2
g(α)	angular response of sensor
H	solar constant (1350 W/m^2)
h	satellite altitude, km
I	radiation intensity, $W/m^2/sr$

i	inclination of orbit plane, deg
J	number of measurements
m	measured flux at satellite altitude, W/m^2
N	square root of number of measurements, $N^2 = J$
Q	radiative flux at top of atmosphere, W/m^2
Q_g	mean global radiative flux at top of atmosphere, W/m^2
R	radius of Earth-atmospheric system, km
r	distance from surface element to satellite, km
v	measurement system error, W/m^2
α	cone angle from satellite nadir to point on surface of Earth, deg
β	clock angle from North about satellite nadir to point on surface of Earth, deg
Δ	incremental change
γ	Earth central angle between surface element and satellite, deg
γ^*	a specific value of γ, deg
ζ	azimuth angle of exiting ray, deg
η	variable of integration
θ	colatitude, deg
λ	directional model parameter
ξ	zenith angle of Sun, deg
ρ	bidirectional function, sr^{-1}
σ	standard deviation, W/m^2
σ^2	variance of measurement system errors, W^2/m^4
ϕ	longitude, deg
ψ	zenith angle of exiting ray, deg
Ω	longitude of ascending node, deg
ω	argument of periapsis or solid angle, deg or sr

Superscripts:

m	model
T	transpose
t	true

Subscripts:

max	maximum
o	initial
s	satellite
$\odot$	Sun

Nomenclature:

FOV_j	field of view for jth zone
WFOV	wide field of view
MFOV	medium field of view

A prime denotes a zonal value. A bar over a symbol denotes a vector and a circumflex ($\hat{}$) over a symbol denotes an estimate.

FORMULATION OF PROBLEM FOR EMITTED RADIATION

The Earth atmosphere system will be approximated by a sphere of radius R. The intensity I of radiation leaving any point on this spherical surface is a function of colatitude θ, longitude ϕ, the zenith angle ψ, and azimuth ζ of the exiting ray. (See fig. 4.) The emitted radiative flux Q at a point on the surface is given by (ref. 6)

$$Q(\theta,\phi) = \int_{\zeta=0}^{2\pi} \int_{\psi=0}^{\pi/2} I(\theta,\phi,\psi,\zeta) \cos\psi \sin\psi \, d\psi \, d\zeta \tag{1}$$

A radiation directional function for emitted radiation $F(\theta,\phi,\psi,\zeta)$ called a limb-darkening function may be defined so that

$$I(\theta,\phi,\psi,\zeta) = \frac{1}{\pi} Q(\theta,\phi) \, F(\theta,\phi,\psi,\zeta) \tag{2}$$

In order that equations (1) and (2) be compatible, it is necessary that F satisfy the normalizing condition

$$\frac{1}{\pi}\int_{\zeta=0}^{2\pi}\int_{\psi=0}^{\pi/2} F(\theta,\phi,\psi,\zeta)\,\cos\psi\,\sin\psi\,d\psi\,d\zeta = 1 \tag{3}$$

For this study F is assumed to have no azimuthal dependence. If the surface is Lambertian, that is, if radiation leaves the surface with equal intensity in all directions, then $F(\theta,\phi,\psi) = 1$.

Now consider a radiation sensor at satellite altitude, as shown in figure 4. The radiation from the Earth incident on the sensor at a colatitude θ_s, longitude ϕ_s, and altitude h is

$$m(\theta_s,\phi_s,h) = \int_{FOV} I(\theta,\phi,\psi,\zeta)\,g(\alpha)\,d\omega \tag{4}$$

where ψ and ζ are functions of the satellite position (θ_s,ϕ_s) and the surface element at the "top" of the atmosphere, ω is the solid angle at the satellite subtended by the surface element, α is the nadir angle at the satellite from the local vertical to the surface element, and the integration is carried out over the field of view FOV. The function $g(\alpha)$ is the angular response of the sensor to incoming radiation. For a perfectly black flat-plate sensor normal to the vertical (nadir looking), $g(\alpha) = \cos\alpha$. Surface properties for other types of sensors can be incorporated in $g(\alpha)$. Although the angular response function may depend on other variables such as azimuthal angle, this paper considers just the class of functions that depend on the nadir angle α. By use of equation (2), equation (4) may be written as

$$m(\theta_s,\phi_s,h) = \frac{1}{\pi}\int_{FOV} Q(\theta,\phi)\,F(\theta,\phi,\psi)\,g(\alpha)\,d\omega \tag{5}$$

Rather than integrate over the solid angle, it is convenient to integrate over the surface element dA or

$$m(\theta_s,\phi_s,h) = \frac{1}{\pi}\int_{FOV} Q(\theta,\phi)\,F(\theta,\phi,\psi)\,g(\alpha)\,\frac{\cos\psi}{r^2}\,dA \tag{6}$$

where r is the distance from the satellite to the surface element. The objective of the data analysis is to solve equation (6) for $Q(\theta,\phi)$.

The data analysis model of the radiation field will consist of 18 latitude zones, each 10° wide, in which the emitted flux is assumed to be constant. Thus, the measurements are modeled as

$$m(\theta_s,\phi_s,h) = \frac{1}{\pi}\sum_{j=1}^{18} Q_j'\int_{FOV_j} F(\theta,\phi,\psi)\,g(\alpha)\,\frac{\cos\psi}{r^2}\,dA + v$$

where Q_j' is the emitted flux in the jth zone and the integration is over the surface area that is in both the field of view and in the jth zone. The

random error in the measurement is denoted by v. Thus, the ith measurement is modeled as

$$m_i = \sum_{j=1}^{18} B_{ij} Q_j' + v_i \tag{7}$$

where B_{ij} is the influence coefficient of Q_j' on the ith measurement and is given by

$$B_{ij} = \frac{1}{\pi} \int_{FOV_j} F(\theta,\phi,\psi)\ g(\alpha)\ \frac{\cos \psi}{r^2}\ dA \tag{8}$$

The variables ψ, α, and r are dependent on the satellite position, θ_s and ϕ_s, at the ith measurement. In matrix form, equation (7) becomes

$$\bar{m} = B\bar{Q}' + \bar{v}$$

where $\bar{m}$ is a column vector of J measurements, $\bar{Q}'$ is a column vector of the 18 zonal fluxes, $\bar{v}$ is a column vector of J measurement errors, and B is the observation matrix with elements B_{ij}.

For a large measurement set ($J >> 18$), it is desired to find the best estimate of $\bar{Q}'$. By the Gauss-Markoff theorem, the best (minimum-variance) linear unbiased estimate of $\bar{Q}'$ is given by the least-squares estimate (ref. 7, p. 349), that is,

$$\hat{\bar{Q}}' = (B^T B)^{-1} B^T \bar{m} \tag{9}$$

where the measurement errors v_i are uncorrelated random variables with mean zero and variance σ^2. Equation (9) together with the necessary supplementary relationship form the basis of the data analysis technique for estimating the emitted flux at the top of the atmosphere.

SIMULATION PROCEDURE FOR EMITTED RADIATION

The data analysis simulation consists of two basic parts, a true Earth-atmosphere radiation system for producing simulated data and a "model" Earth-atmosphere radiation system for the data analysis. A known radiation field is used to generate satellite measurements which are corrupted with random errors and passed to the model system as simulated data. The data analysis technique based on equation (9) is applied to these data and the zonal fluxes are estimated. The comparison is then made between the true flux and the estimated flux. This comparison indicates the accuracy of the data analysis technique. The simulation procedure as outlined above is graphically presented in figure 5.

Simulation of Emitted Radiation Data

There are a number of concerns involved in generating simulated measurements. First, a typical radiation field must be defined over a grid system. The directional dependence F of the radiation must also be defined. In addition, an orbit must be defined along with the number of measurements desired and the sampling strategy. Finally, a numerical integration scheme to obtain the measurements must be established.

The grid system used in this study is illustrated in figure 5 and is an "igloo" grid system. Basically, the surface of the Earth is divided into squares of approximately equal area, the sides of which are latitude and meridian lines. For a 5° by 5° grid, the surface is divided into 5° latitudinal bands and each band is divided into an integral number of areas so that each area is approximately square. The band from 0° to 5° colatitude contains three areas. The band from 5° to 10° colatitude contains nine areas, and so forth. The total number of areas for a 5° by 5° grid is 1654. This is the grid system used throughout the study to simulate measurements.

At each grid area the true emitted flux Φ_i and its true directional dependence $F_i^t(\psi)$ must be defined. The true emitted radiation field for this study was obtained from reference 5 which used the Nimbus III data. A map of the emitted flux is presented in figure 6. The directional functions used are the simple Lambertian function

Lambertian:

$$F(\psi) = \begin{cases} 1 & (0^{\circ} \leq \psi \leq 90^{\circ}) \\ 0 & (\psi > 90^{\circ}) \end{cases} \tag{10a}$$

and the empirical functions derived from the limb darkening functions in reference 5, which are:

Nominal:

$$F(\psi) = \begin{cases} 1.074 \exp\left[0.106(1 - \sec\psi)\right] & (0^{\circ} \leq \psi < 60^{\circ}) \\ 1.074 \exp\left[-0.056 + 0.05(1 - \sec\psi)\right] & (60^{\circ} \leq \psi \leq 90^{\circ}) \\ 0 & (\psi > 90^{\circ}) \end{cases} \tag{10b}$$

Upper:

$$F(\psi) = \begin{cases} 1.03175 & (0^\circ \le \psi < 30^\circ) \\ 1.03175 \exp\left(0.1625\left\{-1 + \exp\left[(\sec 30^\circ - \sec \psi)/2.4\right]\right\}\right) & (30^\circ \le \psi \le 90^\circ) \\ 0 & (\psi > 90^\circ) \end{cases} \quad (10c)$$

Lower:

$$F(\psi) = \begin{cases} 1.106 \exp\left(0.0547(1 - \sec \psi) + 0.09375\left\{\exp\left[2.24(1 - \sec \psi)\right] - 1\right\}\right) & (0^\circ \le \psi \le 90^\circ) \\ 0 & (\psi > 90^\circ) \end{cases} \quad (10d)$$

where the functions are normalized by equation (3). The nominal function is a curve fit to a family of limb darkening functions based on Nimbus III data. The upper and lower functions represent upper and lower bounds, respectively, of the family of functions.

The sampling strategy defines the location of the satellite for each measurement. The satellite orbit can be either elliptical or circular. Most of the numerical results are for a circular orbit with an altitude of 600 km. Figure 7 defines the satellite geometry. The orbital inclination (i) was taken as 100° which corresponds to a common Sun synchronous orbit. The initial argument of periapsis ω_o and the initial longitude of the ascending node Ω_o were taken as 180°. For this study periapsis of a circular orbit is defined arbitrarily by the value given to ω_o. To state the sampling strategy simply, the measurements are uniformly spaced in true anomaly f and longitude. Most satellite measurements are equally spaced in time. The assumption of equal true anomaly spacing is equivalent to equal time spacing for circular orbits. This equivalence also holds approximately for orbits of small eccentricity. The uniform spacing in longitude means that the ascending node is uniformly distributed between 0° and 360° after a sufficient number of orbits. The period of a typical orbit in this study is about 1.5 hours so the satellite passes through 16 ascending nodes a day. It will pass through 16 different nodes the following day, and so forth. Over the period of many days, the distribution of ascending nodes is well represented by the assumption of uniformity.

Although in an actual mission there will be a large number of measurements, it is not necessary to simulate the total number. What is desired is to choose a representative set of simulated data which will allow the data analysis process to be studied. It was decided to generate N^2 measurements, where N measurements are computed on each of N revolutions of the satellite. Thus, the increment between data points is $\Delta f = 360^\circ/N$, and the increment in the orbit node after a complete revolution is $\Delta\Omega = 360^\circ/N$. The argument of periapsis is also incremented after a revolution by $\Delta\omega = \Delta f/N$ so that measurements will be computed at a different set of colatitudes each orbit. The first revo-

lution is described by $\omega = \omega_0 + \Delta\omega$ and $\Omega = \Omega_0 + \Delta\Omega$, and the kth revolution by $\omega = \omega_0 + k\,\Delta\omega$ and $\Omega = \Omega_0 + k\,\Delta\Omega$. In this manner, measurements are computed which are uniformly spaced in true anomaly and longitude. The measurement is then corrupted with a random error to simulate measurement errors. The errors are assumed to be normally distributed with mean zero and variance σ^2 and uncorrelated from measurement to measurement.

The numerical integration scheme used to obtain the simulated data follows directly from the grid system. Since the true emitted flux field is defined by a 5^o by 5^o grid, the measurement (eq. (6)) is approximated by

$$m(\theta_s, \phi_s, h) = \frac{1}{\pi} \sum_{i=1}^{1654} \frac{Q_i A_i \, F_i^t(\psi_i) \, g(\alpha_i) \cos \psi_i}{r_i^2} \tag{11}$$

where the subscript i denotes each grid area. The zenith angle ψ_i, nadir angle α_i, and distance r_i between the satellite and grid area are computed for the center of the grid area defined by the mid-latitude and mid-longitude point. The field of view is defined by $\psi_i \leq 90^o$ since $\psi_i = 90^o$ is the horizon. If $\psi_i < 90^o$, then the entire grid area is considered in the field of view and contributes to the measurement. If $\psi_i > 90^o$, then $F_i^t(\psi_i) = 0$, and this condition eliminates the grid areas not in the field of view. The measurement is then corrupted by adding a normally distributed random error.

Data Analysis Model

The true radiation system and the model radiation system are quite different as seen in figure 5. The modeled radiation field shown consists of 10^o latitude bands each of which represents an area of constant flux. The directional function is modeled as $F^m(\psi)$ and can be any of the directional functions given in equation (10). The superscripts on $F^m(\psi)$ and $F^t(\psi)$ denote that the directional function may be different in the true system and the model system. Thus, the data analysis technique is applied to the measurements to estimate the 18 zonal fluxes which define the model system. The least-squares estimate of these fluxes is obtained from equation (9) where the elements of the B matrix are defined by the integral equation (8). The numerical integration scheme used to evaluate these elements follows from the choice of the 5^o by 5^o grid system; that is, the integral is approximated by

$$B_{kj} = \frac{1}{\pi} \sum_{i} \frac{A_i \, F_i^m(\psi_i) \, g(\alpha_i) \cos \psi_i}{r_i^2} \tag{12}$$

where i ranges over all the grid areas that are in both the field of view and the jth latitude zone. The index k denotes the kth measurement and defines the position of the satellite θ_s and ϕ_s. Notice that the influence coefficient B_{kj} is a function of the modeled direction function $F^m(\psi)$ whereas the simulated measurement (eq. (11)) is a function of the true directional function $F^t(\psi)$. If $F^m(\psi)$ and $F^t(\psi)$ are different, then the esti-

mated flux will be in error and will indicate the sensitivity of estimates to the directional function.

Properties of the emitted flux field which are important data analysis results are (1) the 10^{o} zonal fluxes, (2) the global mean flux, and (3) the equator-to-pole gradient. Sets of simulated measurements were used to estimate these properties by using a variety of assumed directional models, $F^{m}(\psi)$ and $F^{t}(\psi)$, and the results were compared with the true properties. In some cases $F^{m}(\psi)$ and $F^{t}(\psi)$ were the same and in other cases they were different.

The estimate of the flux in the jth latitude zone is defined by $\hat{Q}'_j$ and is the jth element in the vector $\hat{Q}'$ given by equation (9). This quantity is compared with the average true flux which is given by

$$Q'_j = \frac{\sum_i A_i Q_i}{\sum_i A_i} = \frac{\sum_i A_i Q_i}{A'_j} \tag{13}$$

where i ranges over all grid areas in the jth latitude zone. The area and flux of the ith grid area are denoted by A_i and Q_i, respectively, and A'_j is the area of the jth zone. The error in the jth zonal estimate is given by $\hat{Q}'_j - Q'_j$ and the average zonal error is defined by

$$\text{Average zonal error} = \frac{\sum_{j=1}^{18} A'_j \, \text{abs} \left| \hat{Q}'_j - Q'_j \right|}{\sum_{j=1}^{18} A'_j} \tag{14}$$

or in terms of percent the average zonal error is

$$\text{Average zonal error} = \frac{\sum_{j=1}^{18} A'_j \, \text{abs} \left| \frac{\hat{Q}'_j - Q'_j}{Q'_j} \right|}{\sum_{j=1}^{18} A'_j} \tag{15}$$

This is an area weighted average since the zones have different areas. An equatorial zone is much larger than a polar zone and the errors are weighted accordingly. Also, the absolute value of the error is averaged to eliminate cancellation. The average zonal error is a figure of merit for evaluating the data analysis technique.

The global mean flux is another property of interest and is estimated by averaging the zonal estimates; that is,

$$\hat{Q}_g = \frac{\sum_{j=1}^{18} A_j' \hat{Q}_j'}{\sum_{j=1}^{18} A_j'} \tag{16}$$

This estimate is compared with the true global mean flux given by

$$Q_g = \frac{\sum_{j=1}^{18} A_j' Q_j'}{\sum_{j=1}^{18} A_j'} = \frac{\sum_{i=1}^{1654} A_i Q_i}{\sum_{i=1}^{1654} A_i} \tag{17}$$

The definition of the equator-to-pole gradient adopted for this study is the average flux at the equation minus the average flux at the pole. Actually, the surface of the Earth is divided into four zones of equal area as shown in sketch (a) and the average flux for each zone defined. A northern and a

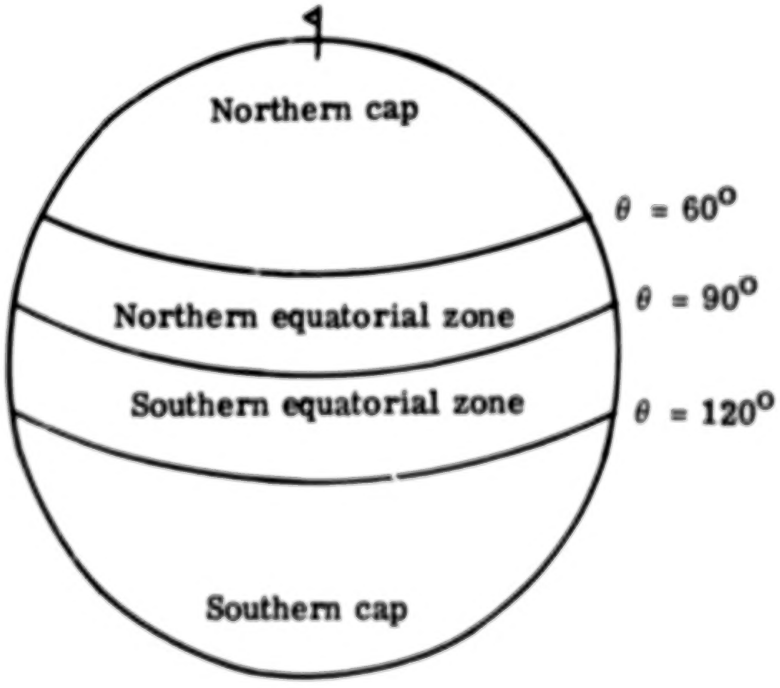

Sketch (a)

southern gradient is defined and the two averaged to yield the equator-to-pole gradient. The average flux in the northern cap is an area-weighted average of six 10° zonal fluxes and is given by

$$Q_{N.cap} = \frac{\sum_{j=1}^{6} A_j' Q_j'}{\sum_{j=1}^{6} A_j'} \tag{18}$$

The average flux for the other three zones is defined in the same manner and the gradient is

$$G = \frac{(Q_{N.eq} - Q_{N.cap}) + (Q_{S.eq} - Q_{S.cap})}{2} \tag{19}$$

The estimate of the equator-to-pole gradient is determined by replacing Q_j' with $\hat{Q}_j'$.

RESULTS AND DISCUSSION FOR EMITTED RADIATION

It is not practical to simulate the large amount of data of an actual mission. The effect of large data sets is to reduce the error in the estimator as a result of improved spatial coverage and to reduce the variance in the estimate due to the measurement errors. This effect is illustrated in figure 8 where the average zonal error is plotted for various data sets. All measurements were made at a satellite altitude of 800 km and the true and model directional functions were Lambertian for all grid areas. As the number of measurements increases, the average zonal error decreases and asymptotically approaches the bias error in the estimation technique. For 3600 measurements, the average zonal error is approximately 0.5 percent. Although it is not necessary to simulate large data sets, the number of measurements should be large enough to eliminate the effect of the location of the measurements. The pattern of the measurements is dictated by the uniform sampling strategy, but the location of the individual measurements depend on the node points of the various orbits defined by Ω_0. For example, if $J = 625$ (25 measurements per orbit times 25 orbits), then the nodes are approximately 14° apart. Thus, $\Omega_0 = 180°$, 183.5°, 187°, 190.5° implies four different measurement sets each containing 625 uniformly spaced measurements. The variation in the average zonal error for these four cases is presented in figure 8. Since this variation due to sampling is unacceptably large, 1296 (36^2) measurements were chosen as an appropriate data set for the simulation results presented herein. The reduction in sampling variation achieved by this is also shown in figure 8.

The random errors added to the computed measurements were all from a normal distribution with mean zero (unbiased) and variance 1 ($\sigma = 1$ W/m^2). This corresponds to a three standard deviation error of 3 W/m^2 or a 1-percent maximum error when the measurement is 300 W/m^2. This is a realistic accuracy for present day WFOV radiometers (ref. 8). The errors in the flux estimates due to unmodeled longitudinal variation of the radiation field, however, far exceed the estimation errors due to random measurement errors. To see this effect, consider the computed measurements on an equatorial orbit. If the zonal flux

were constant, the standard deviation in the measurement would be near 1 W/m^2. The actual standard deviation, however, is 19.7 W/m^2 as a result of the longitudinal variation of the true radiation field. Thus, the relative effect of random measurement errors or the simulation results was small.

One of the major advantages of a simulation study, as compared with an error analysis, is that modeling errors can be investigated more easily. The model radiation system consists of 18 latitude zones of constant flux, which is very different from the true radiation system which consists of 1654 areas of constant flux. This spatial modeling error introduces bias errors into the estimation process. Another modeling error is encountered when $F^t(\psi)$ and $F^m(\psi)$ are different. The data analysis simulation demonstrates the accuracy of the data analysis in the presence of these modeling errors.

Three simulations were performed to determine the estimation errors resulting from the 10^o zonal spatial model. In each case, the true and model directional functions were the same for all grid areas, that is, $F^t(\psi) = F^m(\psi)$. The estimation errors, therefore, resulted only from the spatial modeling error and the random measurement errors. The orbit assumed for these three cases was circular with $h = 600$ km, $i = 100^o$, and $\omega_o = \Omega_o = 180^o$. The sampling strategy assumed was uniform consisting of 1296 measurements based on a flat-plate sensor ($g(\alpha) = \cos \alpha$). In the first case $F^t(\psi)$ and $F^m(\psi)$ were both Lambertian (eq. (10a)). The second case assumed $F^t(\psi)$ and $F^m(\psi)$ were the nominal functions (eq. (10b)). In the third case, part of the surface radiated according to the nominal function and the remainder of the surface was Lambertian. The results from all three simulations were similar.

The second simulation corresponding to the nominal functions is presented in figure 9. The 10^o latitude zone estimates of the flux are plotted as a function of latitude and compared with the true zonal flux (eq. (13)). These estimates represent the actual distribution very well. Furthermore, when used to estimate the global mean (eq. (16)), the error is less than 0.01 percent. This increase in accuracy results because the resolution is better for large areas than for small areas and because a flat-plate WFOV sensor is well suited to measure the global average. In summing to get a global mean, many of the errors in the zonal estimates cancel as can be seen by the alternating signs on the errors. The underlying reasons for these alternating signs and the cancellation are discussed in reference 4. The high degree of accuracy for the global mean results partially because the error in the measurements is unbiased. If the measurements were biased, then the global mean would be biased accordingly. The error in the equator-to-pole gradient was 1.22 percent.

These three cases demonstrated that the spatial resolution obtained from a set of WFOV measurements is smaller than the instrument field of view and that the flat-plate WFOV sensor is well suited to measure both zonal fluxes as well as the global mean flux. The zonal flux estimates, based on zones of constant flux, represent the average of the true fluxes over a zone. This results from the nature of the WFOV sensor and the uniform sampling strategy. The estimation process worked equally well for uniform directional functions (Lambertian) and nonuniform directional functions (limb darkening). Defining different directional functions for different areas of the surface caused no problem in estimation.

A fourth simulation similar to the first (Lambertian) case was performed to test the sensitivity of results to orbit parameters. This case used an elliptical orbit with a periapsis altitude of 600 km and an apoapsis altitude of 800 km. Accuracies obtained were similar to those of the first three cases.

The effect of directional function model errors on the emitted flux estimates was also studied. When $F^t(\psi)$ and $F^m(\psi)$ are different, the result is a bias of the zonal estimates. These biases do not become negligible with an increasing number of measurements. Several simulations were performed to study these biases for different directional functions and the results are presented in table I. In the first simulation, the true directional function is assumed to be the nominal function and the model function is Lambertian. This simulation represents the situation where the directional dependence of the radiation field is ignored and is assumed to be uniform in the data analysis. For this case with 1296 measurements the average zonal error is biased by 0.70 percent or 1.67 W/m^2 and the global mean error remains small. The equator-to-pole gradient is biased 1.65 percent. The next two simulations represent a more reasonable approach to modeling which assumed the nominal function for $F^m(\psi)$ whereas $F^t(\psi)$ was taken as the upper and lower limb darkening function, respectively. If one assumes that these simulations establish reasonable bounds on the bias error due to directional function modeling, then these two cases indicate that the average zonal error will be less than 1.37 W/m^2 if the radiation is modeled by the nominal limb darkening function. The next simulation was presented previously in figure 9 and showed that perfect directional modeling ($F^t(\psi) = F^m(\psi)$) results in a 1.30-W/m^2 zonal error. This error is mainly due to the spatial modeling error which introduces a bias in the estimates; that is, the longitudinal variation in the radiation field is not modeled. The random error in the measurements also contributes to this error. For example, if the true radiation field were constant within a zone, then the average zonal error would be reduced from 1.30 W/m^2 to 0.24 W/m^2. This remaining error is the result of measurement error alone and approaches zero with increasing measurements at the rate $1/\sqrt{J}$. In addition, if the measurements were error free, then the average zonal error would be zero. The worst case which compares the true lower function and the model Lambertian function has an error of 1.76 W/m^2 which is only 0.46 W/m^2 above that which could be expected from perfect directional modeling. Finally, table I shows that an elliptical orbit introduces no additional problems.

Three error sources have been defined and studied. The spatial modeling error and the directional modeling error cause biases in the zonal flux estimates. The random measurement error causes a random error in the zonal flux estimate which tends to zero with increasing number of measurements. The errors caused by these three error sources interact with each other to produce the final results. This interaction must be considered when interpreting the results of table I. Nevertheless, these simulations imply that the error associated with modeling the radiation field as 18 latitude zones of constant magnitude flux is greater than the error associated with modeling the directional dependence. This implies that a finer resolution spatial model would be beneficial for obtaining zonal flux estimates.

FORMULATION OF PROBLEM FOR REFLECTED RADIATION

The major difference between the formulation of simulations for emitted radiation and reflected radiation is the inclusion of the Sun as the radiation source for reflected radiation. The intensity I of radiation reflected by any point at the top of the atmosphere is a function of colatitude θ, longitude ϕ, the zenith angle ψ of the reflected ray, the zenith angle ξ of the Sun, and the azimuth ζ of the reflected ray relative to the Sun. The reflected flux Q at the point is given by

$$Q(\theta,\phi,\xi) = \int_{\zeta=0}^{2\pi} \int_{\psi=0}^{\pi/2} I(\theta,\phi,\psi,\zeta,\xi) \cos\psi \sin\psi \, d\psi \, d\zeta \tag{20}$$

A radiation directional function $\rho(\theta,\phi,\psi,\zeta,\xi)$, called a bidirectional reflectance function, may be defined by

$$I(\theta,\phi,\psi,\zeta,\xi) = Q(\theta,\phi,\xi) \, \rho(\theta,\phi,\psi,\zeta,\xi) \tag{21}$$

In order that equations (20) and (21) be compatible, it is necessary that ρ satisfy the normalizing condition

$$\int_{\zeta=0}^{2\pi} \int_{\psi=0}^{\pi/2} \rho(\theta,\phi,\psi,\zeta,\xi) \cos\psi \sin\psi \, d\psi \, d\zeta = 1 \tag{22}$$

Also, the reflected flux can be modeled as

$$Q(\theta,\phi,\xi) = \begin{cases} H \, a(\theta,\phi) \cos\xi & (0^\circ \le \xi \le 90^\circ) \\ 0 & (90^\circ < \xi \le 180^\circ) \end{cases} \tag{23}$$

where H is the solar constant and $a(\theta,\phi)$ is albedo at the top of the atmosphere. Note that albedo is assumed to vary spatially but not temporally. Thus, the diurnal effect of reflected flux is modeled by $\cos\xi$ and allows for variation only due to the rising and setting of the Sun. The radiation data then will be analyzed by the parameter estimation technique to produce an albedo map at the top of the atmosphere which is related to reflected flux by equation (23) depending on the Sun's location. To proceed, the measurement is given by

$$m(\theta_s,\phi_s,\theta_\odot,\phi_\odot,h) = \int_{FOV} I(\theta,\phi,\psi,\zeta,\xi) \, g(\alpha) \, d\omega$$

where ω is the solid angle at the satellite subtended by the surface element at the top of the atmosphere and $\theta_\odot$ and $\phi_\odot$ denote the position of the Sun. Substitution of equations (21) and (23) yields

$$m(\theta_s,\phi_s,\theta_\odot,\phi_\odot,h) = \int_{FOV} H \, a(\theta,\phi) \cos\xi \, \rho(\theta,\phi,\psi,\zeta,\xi) \, g(\alpha) \, d\omega$$

or

$$m(\theta_s,\phi_s,\theta_\odot,\phi_\odot,h) = \int_{POV} H\, a(\theta,\phi)\, \cos\xi\, \rho(\theta,\phi,\psi,\zeta,\xi)\, g(\alpha)\, \frac{\cos\psi}{r^2}\, dA$$

where r is the distance from the satellite to the surface element dA. The data analysis model of the albedo field will consist of 18 latitude zones, each with constant albedo a_j'. Thus, the measurements are modeled as

$$m(\theta_s,\phi_s,\theta_\odot,\phi_\odot,h) = \sum_{j=1}^{18} a_j' \int_{POV_j} H \cos\xi\, \rho(\theta,\phi,\psi,\zeta,\xi)\, g(\alpha) \frac{\cos\psi}{r^2}\, dA + v$$

where the integration is over the surface area that is in both the field of view and the jth zone. The random error in the measurement is v. Thus, the ith measurement is modeled as

$$m_i = \sum_{j=1}^{18} B_{ij} a_j' + v_i$$

where B_{ij} is the influence coefficient of a_j' on the ith measurement and is given by

$$B_{ij} = \int_{POV_j} H \cos\xi\, \rho(\theta,\phi,\psi,\zeta,\xi)\, g(\alpha)\, \frac{\cos\psi}{r^2}\, dA \qquad (24)$$

In matrix notation

$$\bar{m} = B\bar{a}' + \bar{v}$$

where $\bar{m}$ is a column vector of J measurements, $\bar{a}'$ is a column vector of the 18 zonal albedos, $\bar{v}$ is a column vector of J measurement errors, and B is the observation matrix with elements B_{ij} (eq. (24)). According to equation (9), the least-squares estimate of albedo is

$$\hat{\bar{a}}' = (B^T B)^{-1} B^T \bar{m} \qquad (25)$$

and the resulting estimate of flux is given by equation (23).

SIMULATION PROCEDURE FOR REFLECTED RADIATION

The simulation procedure for reflected radiation is very similar to the procedure for emitted radiation. Consider a true Earth-atmosphere radiation system and a model Earth-atmosphere radiation system and compare the true flux with the estimated flux. The estimated parameter, however, is albedo which is related to flux through dependence upon the position of the Sun.

The true system consists of a 5^{o} by 5^{o} grid system of 1654 grid areas. The true albedo for this study was obtained from reference 5 which used the Nimbus III data.

The bidirectional function $\rho(\psi, \zeta, \xi)$ has been assumed to vary only with the zenith of the Sun, the zenith of the reflected ray, and the azimuth between the two and does not vary with latitude or longitude. A sketch (sketch (b)) of the geometry at a point P at the top of the atmosphere shows the three variables where

$$0^{o} \leq \psi \leq 90^{o}$$

$$0^{o} \leq \xi \leq 90^{o}$$

$$0^{o} \leq \zeta \leq 360^{o}$$

The notation "forward" denotes the forward reflections of the Sun.

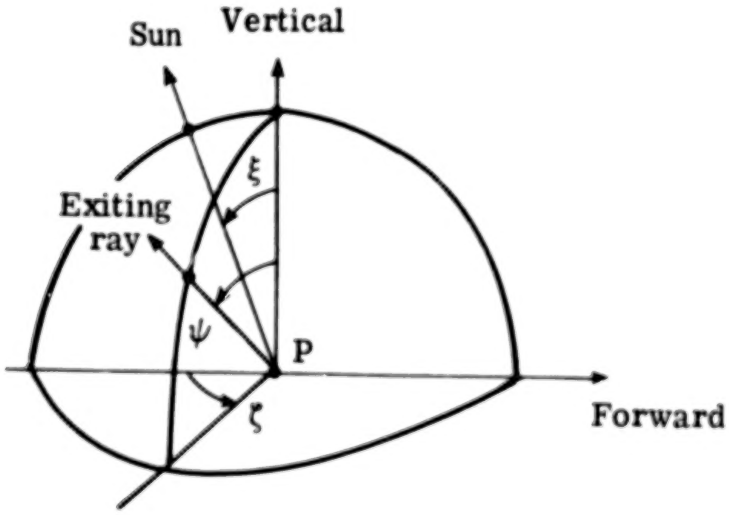

Sketch (b)

The functional form for $\psi \leq 90^{o}$ is given by

$$\rho(\psi,\zeta,\xi) = \frac{N(\xi)}{\pi}\left\{1 + C_1(\sin\xi)^{C_2} + C_3 \sin^{2/3}\xi + C_4 \sin^{6}\xi \sin^{2}\psi\,(\cos^{2}\zeta + C_5 \sin^{2}\zeta) - C_6 \cos\zeta\sqrt{1 - \sin^{2}\zeta}\,\sin^{2}\xi \sin\psi\left[1 + \frac{1}{2}(1 + 3\cos 4\xi)\sin^{2}\zeta\right]\right\}^{-1} \tag{26}$$

where

$$C_1 = 1.5853$$

$$C_2 = 13.4646$$

$$C_3 = -0.01717$$

$$C_4 = -1.856$$

$$C_5 = 0.3046$$

$$C_6 = -0.357$$

and $N(\xi)$ is the normalizing function so equation (22) is satisfied. A graph of $N(\xi)$ is presented in figure 10 and $\rho(\psi,\zeta,\xi)$ is presented in figure 11. The bidirectional function is set equal to zero for $\psi > 90^{\circ}$. This bidirectional function is an empirical model based on the data of reference 5. To simulate bidirectional modeling error, a family of functions has been defined and is given by

$$B(\psi,\zeta,\xi) = \lambda\, \rho(\psi,\zeta,\xi) + (1 - \lambda)\frac{1}{\pi} \qquad (0 \leq \lambda \leq 1) \tag{27}$$

The bidirectional function B is a composite of the empirical model and a diffuse model and represents a linear variation with λ between the two models. Thus, to simulate bidirectional modeling error, one can generate the measurements with $\lambda = 1$ (empirical model) and estimate the albedo with $\lambda = 0$ (diffuse model) or any other combination of λ values. The error in the estimate of albedo will then indicate the relationship between modeling errors and albedo estimates.

For all the simulations presented here, the Sun's position has been assumed to be fixed with respect to the orbital plane. If the orbit were Sun synchronous, then this would be the case and the change in the orbit node with respect to the Sun would be zero. For low inclination orbits, this assumption is valid only for a few days. Since the true albedo field is constant with time (that is, it has no diurnal variation), the diurnal variation of the flux field is deterministic and a result of the Sun elevation alone. Thus, data at one Sun angle or one local time is sufficient to estimate the albedo field. Fixing the Sun position relative to the orbital plane, therefore, is consistent with the assumption of a non-time-dependent albedo. Nevertheless, different Sun positions are considered to determine their effect upon the albedo estimates.

The numerical integration scheme used to obtain the simulated reflected flux measurement is based on the 5° by 5° grid system and is given by

$$m(\theta_s,\phi_s,\theta_\odot,\phi_\odot,h) = \sum_{i=1}^{1654} \frac{H \cos \xi_i\, \rho(\psi_i,\zeta_i,\xi_i)\, g(\alpha_i) \cos \psi_i\, A_i\, a_i}{r_i^2} \tag{28}$$

where the subscript i denotes each grid area, the bidirectional function has been assumed equal to ρ for all grid areas, and a_i is the true albedo for each grid area. The wide field of view is defined by $\psi_i \leq 90^\circ$. The 5° by 5° grid system is also used to approximate the influence coefficients (eq. (24)); that is,

$$B_{kj} = \sum_i \frac{H \cos \xi_i \, g(\alpha_i) \cos \psi_i A_i}{r_i^2} \left[\lambda \rho(\psi_i, \zeta_i, \xi_i) - \frac{(1 - \lambda)}{\pi} \right] \tag{29}$$

where i ranges over all the grid areas that are in both the kth field of view and the jth latitude zone. The influence coefficients reflect directional modeling errors which are controlled by the parameter λ.

The estimates of the zonal albedos are given by equation (25) and they are compared with the true zonal albedos given by

$$a'_j = \frac{\sum_i A_i a_i}{\sum_i A_i} \tag{30}$$

With the position of the Sun known, one can convert the average zonal albedo into the average zonal flux. This relationship is derived in the appendix. If the Sun is in the equatorial plane, then the average zonal flux is

$$Q'_j = \frac{a'_j F(\Delta\theta - \sin \Delta\theta + 2 \sin \Delta\theta \sin^2 \bar{\theta}_j)}{4\pi \sin\left(\frac{\Delta\theta}{2}\right) \sin \bar{\theta}_j} \tag{31}$$

where $\bar{\theta}_j$ is the mid-latitude of the jth zone or $\bar{\theta}_j = \theta_j + (\Delta\theta/2)$. The estimates of zonal flux are obtained by evaluating equation (31) with $a'_j = \hat{a}'_j$. These fluxes are then used to evaluate the average zonal error (eqs. (14) and (15)), the global mean flux (eqs. (16) and (17)), and the equator-to-pole gradient (eqs. (18) and (19)).

RESULTS AND DISCUSSION FOR REFLECTED RADIATION

The model radiation system for the reflected simulation study consists of 18 latitude zones of constant albedo. The results from a typical simulation with no directional modeling errors are presented in figure 12. The estimate of the albedo field is seen to represent the true field very well. Also shown is the reflected flux for the Sun in the equatorial plane. The odd number of measurements results from considering 2500 uniformly spaced measurements, 917 of which were in total darkness. Thus, only 1583 measurements were used to estimate the zonal albedos. The average zonal flux error for this simulation was 1.24 W/m^2 and the global mean error was -0.17 W/m^2. The equator-to-pole gradient was in error by -0.49 W/m^2. Since the gradient is a difference between

fluxes, its error is not reflected directly by the zonal or global errors. For example, if the albedo estimates were uniformly high, then the zonal and global errors would be affected directly while the gradient would only be indirectly affected. Suppose the situation was such that the zonal errors canceled each other and the global error was zero. If the zonal errors were evenly distributed over the globe, then the gradient error would be minimal. However, if the zonal estimates were high in the polar regions and low in the equatorial region, then the gradient error would be much larger than one would expect by considering only the zonal and global errors.

The directional modeling error has been studied by assuming a bidirectional model that varies linearly with λ between the empirical bidirectional model and a diffuse model. The simulated measurements were computed by using $\rho(\psi,\zeta,\xi)$ (eq. (28)) and the albedos were estimated by using

$$B(\psi,\zeta,\xi) = \lambda\rho(\psi,\zeta,\xi) + (1 - \lambda)\frac{1}{\pi}$$

as the directional model (eq. (29)). The diffuse assumption corresponds to $\lambda = 0$ and perfect directional modeling corresponds to $\lambda = 1$. Results of simulations for various λ values are presented in figure 13. As would be expected, the global and zonal errors are reduced with better directional modeling. They exhibit errors, however, even for perfect directional modeling. These errors are the result of the spatial modeling error; that is, the error associated with representing the albedo field by 18 zones of constant albedo. The gradient error exhibits a behavior much different from the global or zonal errors. It has a positive error for $\lambda = 0$ and a negative error for $\lambda = 1$.

For the reflected radiation simulations discussed, the position of the Sun was assumed to be at a right ascension and declination of zero; that is, the Sun was assumed to be in the orbital plane and at the equator. This assumption corresponds to a noon Sun synchronous orbit during equinox. The effect of changing the right ascension of the Sun to 45° is presented in figure 14. This case is the same as the case presented in figure 12 except $\phi_{\odot} = 45°$. The individual zonal errors are plotted against latitude for Sun right ascension of zero and 45°. The conclusion is that the right ascension of the Sun does not significantly change the results of the simulation. Hence, the right ascension of the Sun was assumed to be zero. If the declination of the Sun is changed, one of the poles will be in darkness and an albedo estimate of that pole is impossible. Six months later, however, the situation is reversed and the other pole is in darkness. Thus, over a 6-month period both poles are observable. For this reason the declination of the Sun was assumed to be zero throughout this study so that both poles would be observable.

RESULTS AND DISCUSSION FOR MEDIUM FIELD OF VIEW SENSOR

All the simulation results presented thus far have been for a wide field of view radiometer which receives radiation from all points on the Earth's surface from nadir to horizon. If the field of view is restricted, it becomes a medium field of view (MFOV) radiometer. The analysis of this instrument using

the simulation procedure outlined previously is straightforward. The only change is that a smaller surface area is viewed by the instrument. Since the sensor is still a nadir pointing instrument, its field of view can be defined by either α the cone angle from satellite nadir to the edge of the field of view or by γ the Earth central angle (fig. 4). Previously, the field of view was defined by $\psi \leq 90^{\circ}$. The relationship between these two angles for various satellite altitudes is presented in figure 15. The curve labeled $\gamma = \gamma^*$ corresponds to the WFOV sensor and at an altitude of 600 km, $\gamma^* = 23.93^{\circ}$ and $\alpha = 66.06^{\circ}$. Of course, γ^* changes for different altitudes. The other two curves represent a constant γ. For example, if $\gamma = 5^{\circ}$ and $h = 600$ km, then $\alpha = 41.68^{\circ}$. Another notation used to describe the MFOV sensor is the total Earth central angle (ECA) of the field of view or ECA = 2γ. All the simulations reported in this section are for an ECA of 10°. Results from a typical MFOV simulation for emitted radiation are shown in figure 16. Directional modeling errors were not considered for this case. It can be seen that the estimated flux field matches the real field well except at the North Pole. The average zonal error is nearly the same as for the perfect modeling WFOV case of figure 9. The global mean error and the gradient error, however, are larger for the MFOV case. When the directional modeling errors were considered, errors in the estimate of the zonal flux, global mean, and gradient increased even more significantly. The results are presented in table II. Recall that the WFOV flat-plate sensor is well suited to measure the global mean flux independent of the directional function. This is not the case for MFOV sensors. In fact, since the MFOV sensor does not receive radiation from high zenith angles, the global estimate is biased depending on the assumed directional functions. These biases also affect the accuracy of the zonal estimates. An interesting result is that the equator-to-pole gradient can be estimated better with a WFOV sensor than with a MFOV sensor. This condition possibly could result from the reduced spatial sampling of the MFOV sensor.

The same type of analysis for the estimation of the albedo field was performed for the MFOV as for the WFOV sensor. The results of a typical simulation are presented in figure 17 and are very similar to the WFOV sensor results (fig. 12). The sensitivity of these estimates to directional modeling errors for reflected radiation is shown in figure 18. These errors are generally larger than the WFOV errors except for perfect directional modeling ($\lambda = 1$). Thus, the WFOV and the MFOV estimates are comparable for perfect modeling. However, the MFOV sensor is much more sensitive to directional modeling errors than the WFOV sensor.

CONCLUDING REMARKS

A parameter estimation technique has been defined to analyze wide field of view (WFOV) radiometer measurements to obtain radiation flux estimates at the top of the atmosphere. A computer simulation of the data analysis technique has been performed for both Earth-emitted and reflected radiation. Results were also obtained for a medium field of view (MFOV) radiometer.

The error sources considered in estimating the emitted flux at the top of the atmosphere for WFOV measurements are the assumed limb darkening function, the assumed spatial model of the flux field, and the random error in the

measurement. If the flux field is modeled as 10° zonal bands of constant flux and a nominal limb darkening function is chosen, the average zonal error is 1.37 W/m^2. Most of this error is attributed to the spatial modeling. A perfect limb darkening model only reduces the zonal error to 1.30 W/m^2. If the zones are in fact regions of constant flux, the zonal error is reduced to the measurement error which is 0.24 W/m^2 for a sample size of 1296 measurements and decreases to zero with increased measurements. The spatial modeling error and the limb darkening error, however, result in an estimate bias that does not decrease to zero with increased measurements. The global mean error was found to be insensitive to the spatial and limb darkening models and was less than 0.05 W/m^2. The equator-to-pole gradient can be estimated to within 1.0 W/m^2.

The error sources considered for estimating the reflected flux at the top of the atmosphere from WFOV measurements are the same as those for the emitted flux. If the spatial model is assumed to be 10° zonal bands of constant albedo and the directional dependence of the flux is taken to be diffuse instead of bidirectional, then the average zonal error is 2.92 W/m^2, the global mean error is -1.44 W/m^2, and the gradient error is 0.50 W/m^2. Removing the directional modeling error by choosing the correct bidirectional function reduces these errors. For perfect directional modeling, the zonal error is 1.24 W/m^2, the global mean error is -0.17 W/m^2, and the gradient error is -0.49 W/m^2.

Results have been obtained for a medium field of view radiometer. Instead of viewing all points on the surface from nadir to the horizon, the MFOV is restricted to an Earth central angle of 10°. For perfect directional modeling, the WFOV and MFOV estimates of the zonal and global flux are approximately the same. However, the flux estimates from MFOV measurements are more sensitive to directional modeling errors than are the flux estimates from WFOV measurements. For example, the emitted flux global mean could be in error by as much as 5.55 W/m^2 for MFOV as compared with 0.05 W/m^2 for WFOV. This error also affects the zonal error for MFOV. The emitted flux equator-to-pole gradient can be estimated better with a WFOV sensor than with a MFOV sensor. This is in part a consequence of the reduced field of view and the large flux errors at the poles exhibited by the MFOV estimates. Results for the MFOV reflected flux estimates are also very sensitive to directional modeling errors.

Langley Research Center
National Aeronautics and Space Administration
Hampton, VA 23665
March 29, 1978

APPENDIX

AVERAGE REFLECTED FLUX OVER AN AREA

Consider the average reflected flux over an area A given by

$$Q = \frac{\int_A Q \, dA}{\int_A dA} = \frac{\int_A aH \cos \xi \, dA}{\int_A dA} \tag{A1}$$

where a is albedo, H is the solar constant, and ξ is the zenith of the Sun. For a latitude zone defined by $\theta_i \leq \theta \leq \theta_i + \Delta\theta$ and $0 \leq \phi < 2\pi$, write

$$A_i' = \int_A dA = \int_{\phi=0}^{\phi=2\pi} \int_{\theta=\theta_i}^{\theta=\theta_i+\Delta\theta} R^2 \sin \theta \, d\theta \, d\phi$$

$$A_i' = 4\pi R^2 \sin\left(\frac{\Delta\theta}{2}\right) \sin \bar{\theta}_i \tag{A2}$$

where $\bar{\theta}_i = \theta_i + (\Delta\theta/2)$ is the average colatitude and R is the radius of the Earth-atmospheric system. Before the average flux can be computed from equation (A1), one needs an expression for $\cos \xi$ in terms of ϕ and θ. The unit vector to the Sun is

$$\hat{X}_\odot = (\sin \theta_\odot \cos \phi_\odot, \sin \theta_\odot \sin \phi_\odot, \cos \theta_\odot)$$

and the unit vector normal to the surface element dA is

$$\hat{X}_A = (\sin \theta \cos \phi, \sin \theta \sin \phi, \cos \theta)$$

Thus,

$$\cos \xi = \hat{X}_\odot \cdot \hat{X}_A$$

$$= \sin \theta_\odot \sin \theta \cos \phi_\odot \cos \phi + \sin \theta_\odot \sin \theta \sin \phi_\odot \sin \phi + \cos \theta_\odot \cos \theta$$

$$= \sin \theta_\odot \sin \theta \cos (\phi - \phi_\odot) + \cos \theta_\odot \cos \theta$$

and for a zone of constant albedo a', one has

$$Q' = \frac{1}{A'} \int_A a'H \cos \xi \, dA$$

APPENDIX

$$Q' = \frac{a'}{A'} \int_{\phi=0}^{\phi=2\pi} \int_{\theta=\bar{\theta}-(\Delta\theta/2)}^{\theta=\bar{\theta}+(\Delta\theta/2)} H(\sin\theta_\odot \sin\theta \cos(\phi - \phi_\odot) + \cos\theta_\odot \cos\theta) R^2 \sin\theta \, d\theta \, d\phi$$

Since the reflected flux is zero over the dark side of the Earth ($\xi > \pi/2$), one can redefine the variable of integration as $\eta = \phi - \phi_\odot$ and integrate from $-\eta^*$ to η^* where η^* represents the Sun terminator which is considered constant over $\Delta\theta$; that is,

$$Q' = \frac{a'}{A'} \int_{\eta=-\eta^*}^{\eta=\eta^*} \int_{\theta=\bar{\theta}-(\Delta\theta/2)}^{\theta=\bar{\theta}+(\Delta\theta/2)} H(\sin\theta_\odot \sin\theta \cos\eta + \cos\theta_\odot \cos\theta) R^2 \sin\theta \, d\theta \, d\eta$$

$$Q' = \frac{a'}{A'} HR^2 \left[(\Delta\theta - \sin\Delta\theta + 2 \sin\Delta\theta \sin^2\bar{\theta}) \sin\eta^* \sin\theta_\odot + 2\eta^* (\sin\Delta\theta \sin\bar{\theta} \cos\bar{\theta}) \cos\theta_\odot \right] \qquad \text{(A3)}$$

where η^* is defined by $\cos\xi = 0$ or

$$\sin\theta_\odot \sin\theta \cos\eta^* + \cos\theta_\odot \cos\bar{\theta} = 0$$

or

$$\eta^* = \cos^{-1}(\cot\theta_\odot \cot\bar{\theta}) \qquad (0 \leq \eta^* \leq \pi)$$

If the Sun is in the equatorial plane, then $\theta_\odot = \pi/2$, $\eta^* = \pi/2$, and

$$Q' = \frac{a'}{A'} HR^2(\Delta\theta - \sin\Delta\theta + 2 \sin\Delta\theta \sin^2\bar{\theta})$$

and from equation (A2)

$$Q' = \frac{a' HR^2(\Delta\theta - \sin\Delta\theta + 2 \sin\Delta\theta \sin^2\bar{\theta})}{4\pi R^2 \sin\left(\frac{\Delta\theta}{2}\right) \sin\bar{\theta}}$$

$$Q' = \frac{a' H(\Delta\theta - \sin\Delta\theta + 2 \sin\Delta\theta \sin^2\bar{\theta})}{4\pi \sin\left(\frac{\Delta\theta}{2}\right) \sin\bar{\theta}}$$

APPENDIX

It is interesting to note that as the width of the latitude zone becomes small such that $\sin \Delta\theta \sim \Delta\theta$, the average zonal flux is

$$Q' \sim \frac{a'H \sin \bar{\theta}}{\pi} = \frac{Q_{max}}{\pi}$$

or the average zonal flux is approximately equal to the maximum flux at the Sun's meridian divided by π which accounts for the reduction in flux away from the Sun's meridian.

REFERENCES

1. Pina, J. F.; and House, F. B.: An Inversion Method for Computing Radiances and Albedos of Earth-Atmosphere Regions From Wide-Angle Satellite Sensor Measurements. Second Conference on Atmospheric Radiation (Arlington, Va.), American Meteorol. Soc., Oct. 1975, pp. 119-122.

2. Smith, G. Louis; and Green, Richard N.: A Technique for Analysis of Low Resolution Measurements of Earth Radiation Budget. Second Conference on Atmospheric Radiation (Arlington, Va.), American Meteorol. Soc., Oct. 1975, pp. 111-114.

3. Smith, G. Louis; and Green, Richard N.: Theoretical Analysis of Wide Field of View Radiometer Measurements of Earth Energy Budget. Fifth Annual Remote Sensing of Earth Resources Conference (Tullahoma, Tenn.), Mar. 1976.

4. Smith, G. Louis; Green, Richard N.; and Campbell, G. G.: A Statistical Interpretation Technique for Wide Angle Radiometer Measurements of Earth Energy Budget. Fourth Conference on Probability and Statistics in Atmospheric Sciences, American Meteorol. Soc., Nov. 1975, pp. 171-176.

5. Raschke, Ehrhard; Vonder Haar, Thomas H.; Pasternak, Musa; and Bandeen, William R.: The Radiation Balance of the Earth-Atmosphere System From Nimbus 3 Radiation Measurements. NASA TN D-7249, 1973.

6. Siegel, Robert; and Howell, John R.: Thermal Radiation Heat Transfer. Volume I - The Blackbody, Electro-Magnetic Theory, and Material Properties. NASA SP-164, 1968.

7. Mood, Alexander M.; and Graybill, Franklin A.: Introduction to the Theory of Statistics. Second ed. McGraw-Hill Book Co., Inc., c.1963.

8. Hickey, J. R.; and Karoli, A. R.: Radiometric Calibrations for the Earth Radiation Budget Experiment. Appl. Optics, vol. 13, no. 3, Mar. 1974, pp. 523-533.

TABLE I.- SENSITIVITY OF WFOV ESTIMATES TO DIRECTIONAL FUNCTION MODEL FOR EMITTED RADIATION

[100° orbit; 1296 measurements; sensor error, 1 W/m^2]

$F^r(\psi)$	$F^m(\psi)$	Global mean error		Average zonal error		Gradient error		Altitude, km	Remarks
		Percent	W/m^2	Percent	W/m^2	Percent	W/m^2		
Nominal	Lambertian	-0.0004	-0.001	0.70	1.67	1.65	0.81	600	No model
Lower	Nominal	-.0094	-.022	.57	1.37	1.16	.57	600	Lower bound
Upper	Nominal	.0188	.045	.45	1.09	1.07	.52	600	Upper bound
Nominal	Nominal	.0073	.017	.54	1.30	1.22	.60	600	Perfect model
Lower	Lambertian	-.0174	-.042	.74	1.76	1.58	.78	600	Worst case
Nominal	Lambertian	.0085	.020	.68	1.62	2.15	1.06	600 × 800	Elliptical orbit

TABLE II.- SENSITIVITY OF MFOV ESTIMATES TO DIRECTIONAL FUNCTION MODEL FOR EMITTED RADIATION

[100° orbit; 1296 measurements; sensor error, 1 W/m^2]

$F^r(\psi)$	$F^m(\psi)$	Global mean error		Average zonal error		Gradient error		Altitude, km	Remarks
		Percent	W/m^2	Percent	W/m^2	Percent	W/m^2		
Nominal	Lambertian	5.40	12.94	5.56	13.31	7.72	3.79	600	No model
Lower	Nominal	1.04	2.49	1.27	3.05	3.04	1.49	600	Lower bound
Upper	Nominal	-2.32	-5.55	2.41	5.76	-.11	-.06	600	Upper bound
Nominal	Nominal	.12	.29	.60	1.43	2.25	1.11	600	Perfect model
Lower	Lambertian	6.37	15.26	6.52	15.62	8.55	4.19	600	Worst case
Nominal	Lambertian	5.34	12.79	5.50	13.17	8.02	3.93	600 × 800	Elliptical orbit

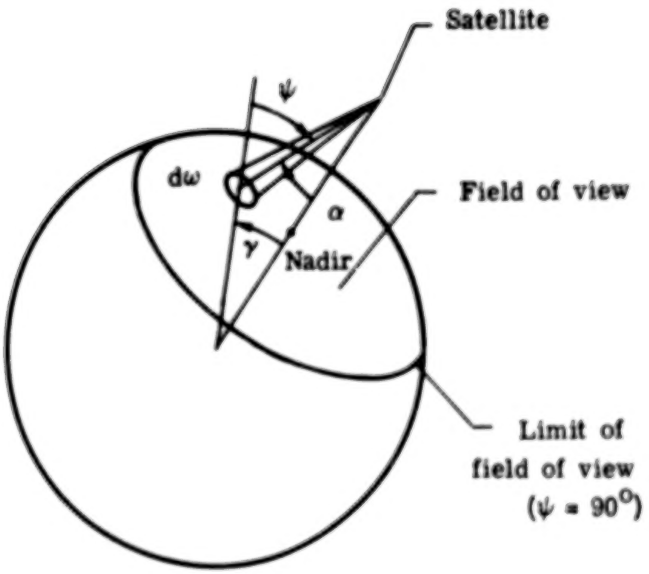

Figure 1.- Wide field-of-view radiometer data analysis problem.

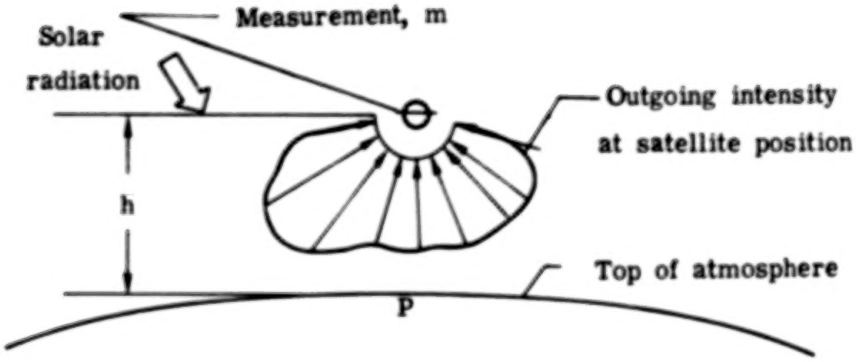

(a) Radiation at satellite altitude.

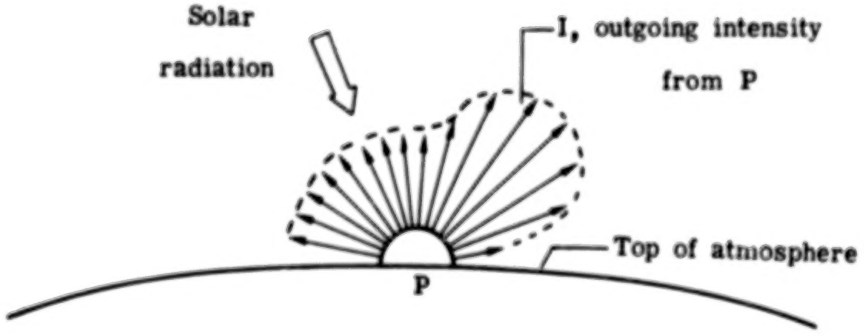

(b) Radiation at top of atmosphere.

Figure 2.- Radiation directionality at top of atmosphere and at satellite altitude.

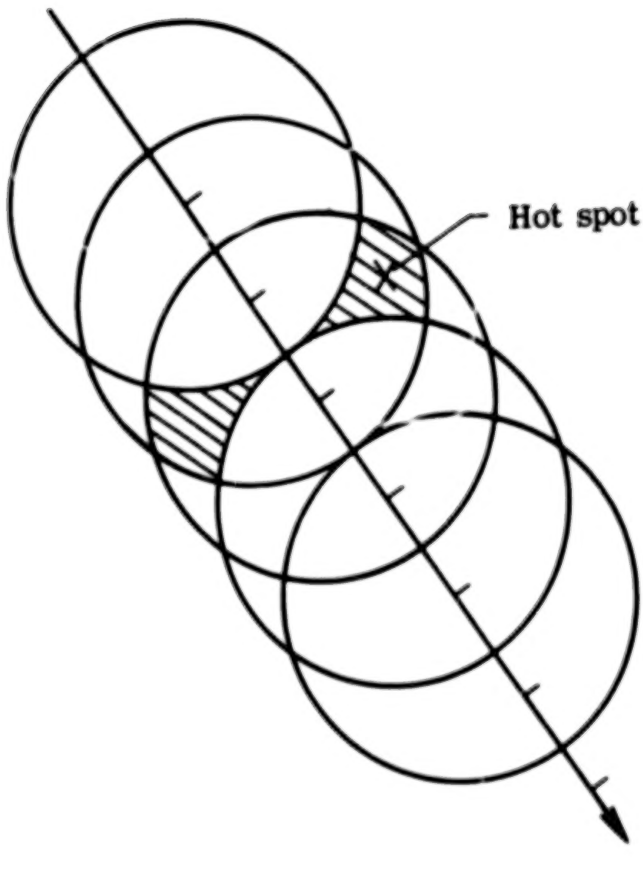

Figure 3.- Information from measurements with overlapping view fields.

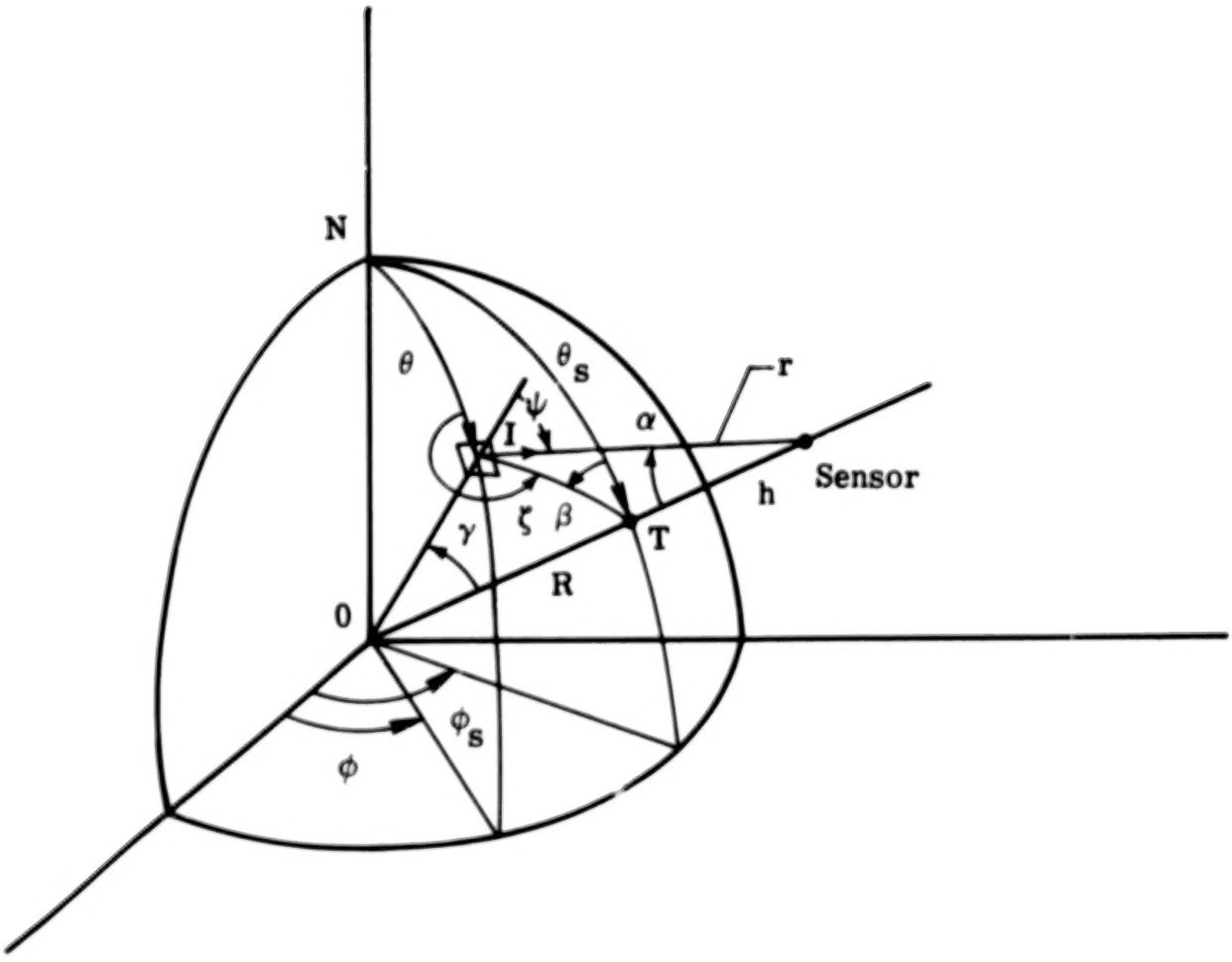

Figure 4.- Earth-satellite geometry.

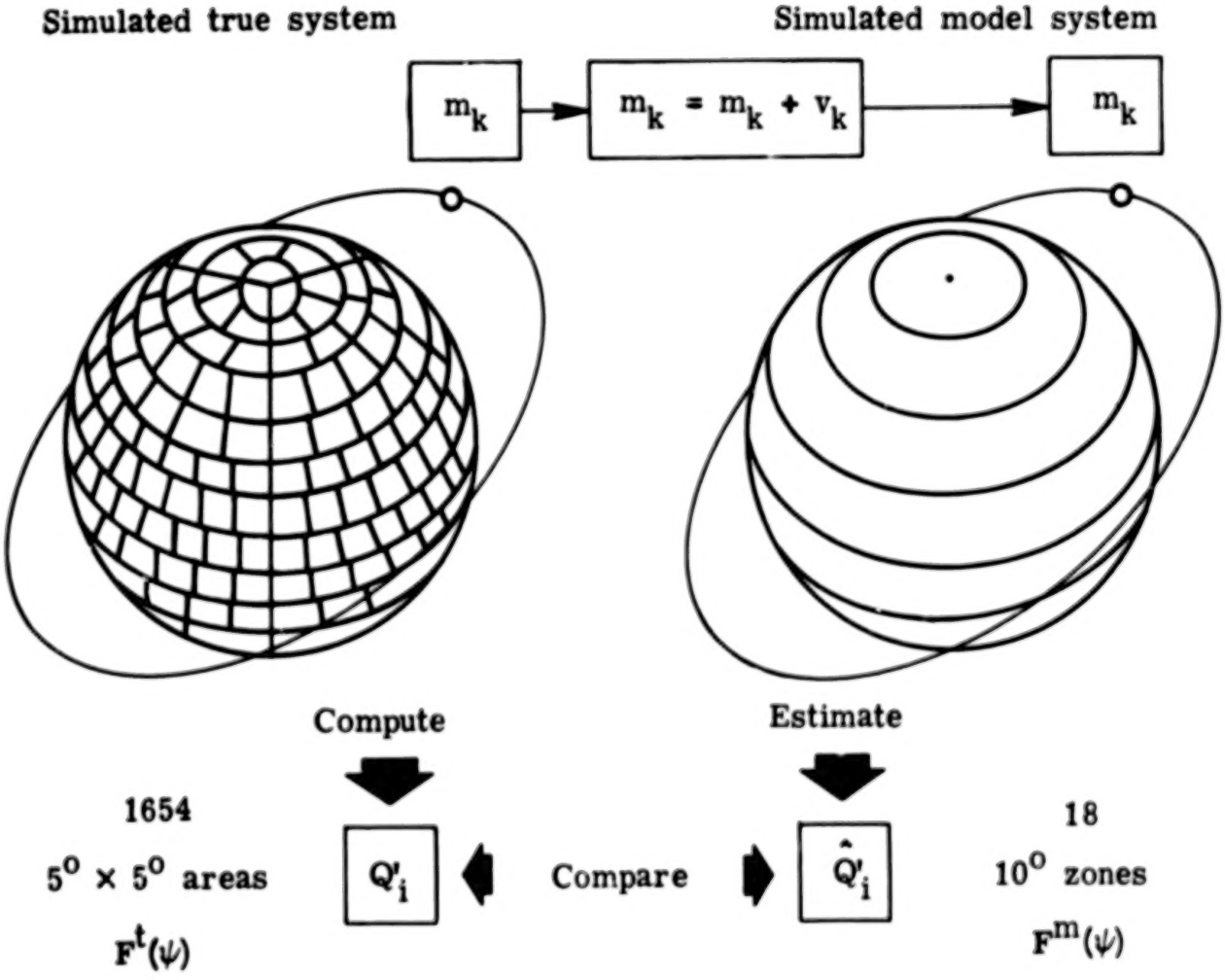

Figure 5.- Simulation of emitted wide field-of-view measurements and analysis.

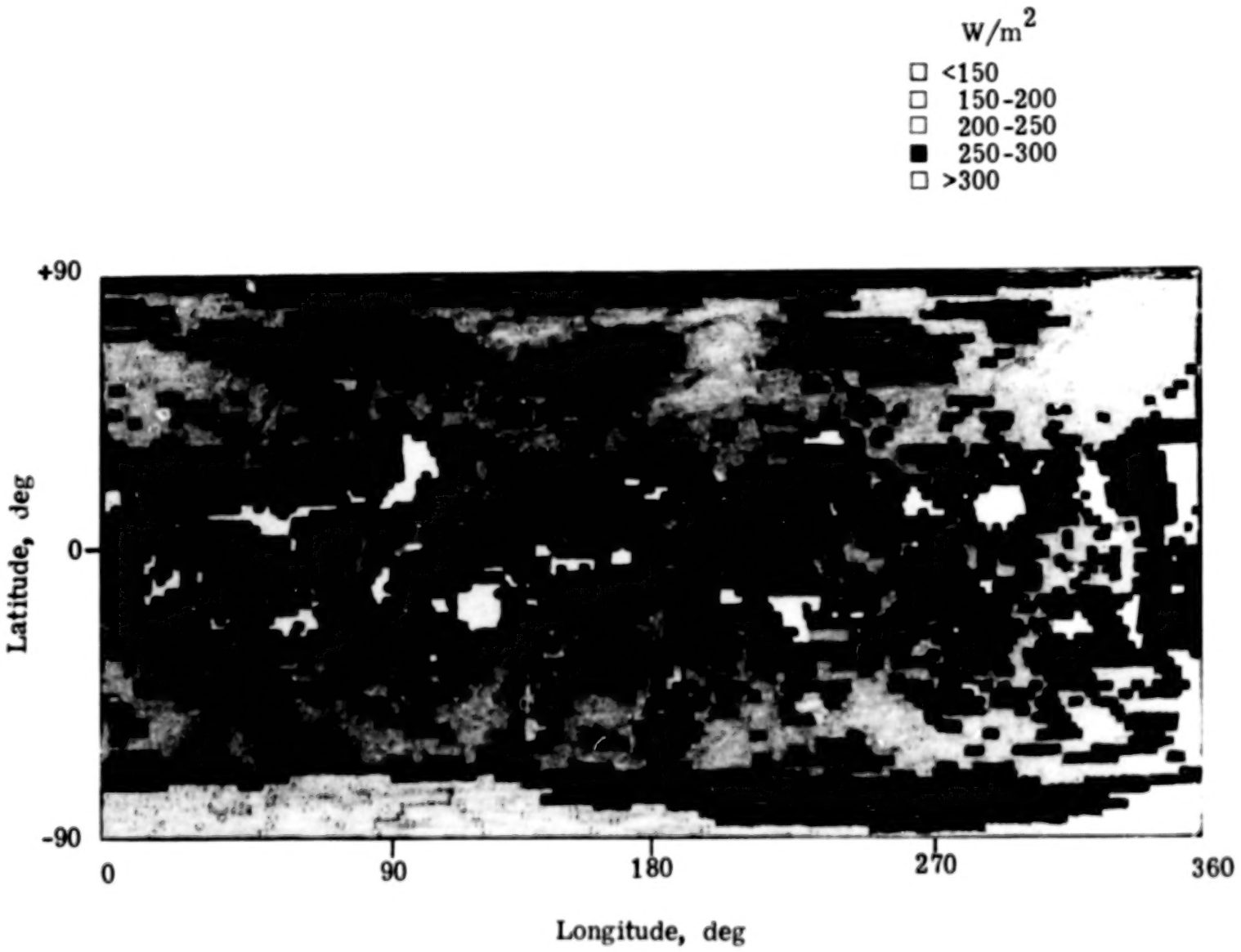

Figure 6.- Earth emitted flux map used in simulation.

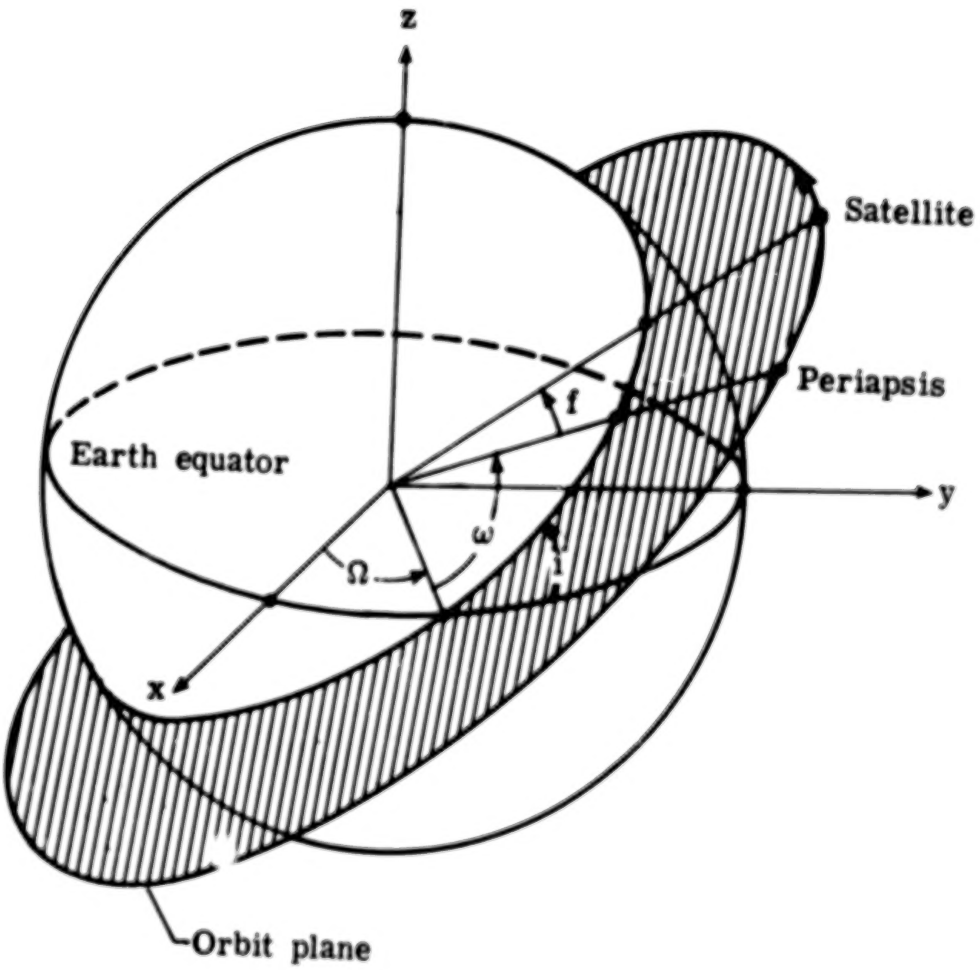

Figure 7.- Orbit geometry.

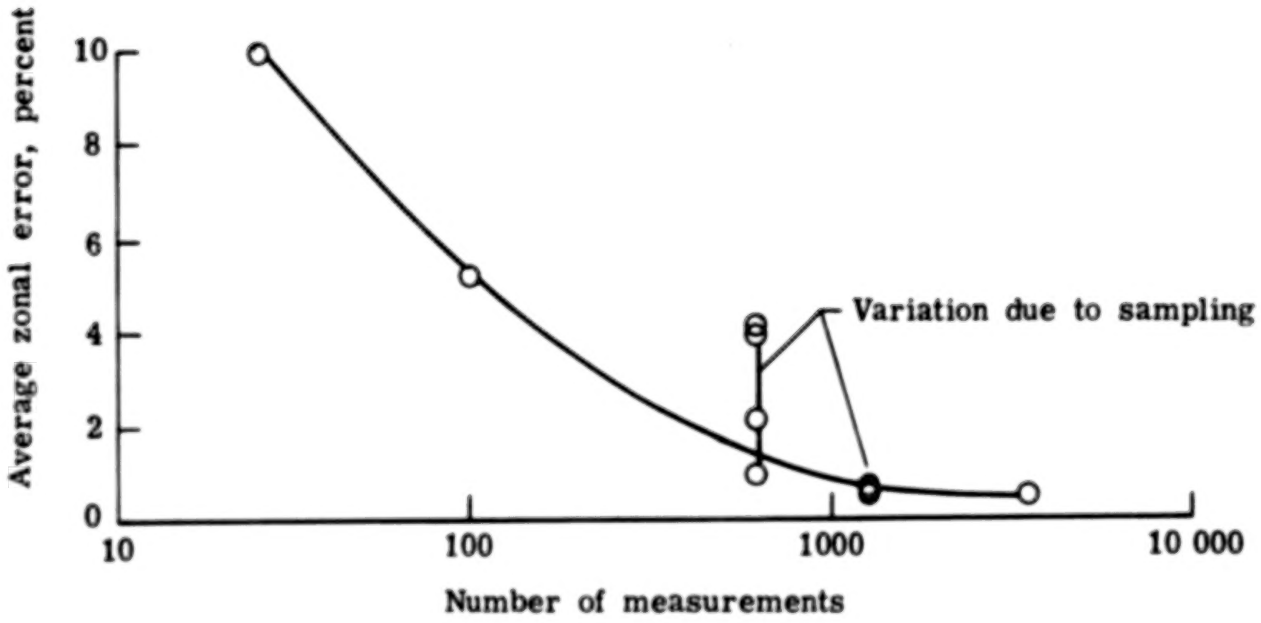

Figure 8.- Variation of average zonal error with number of measurements.

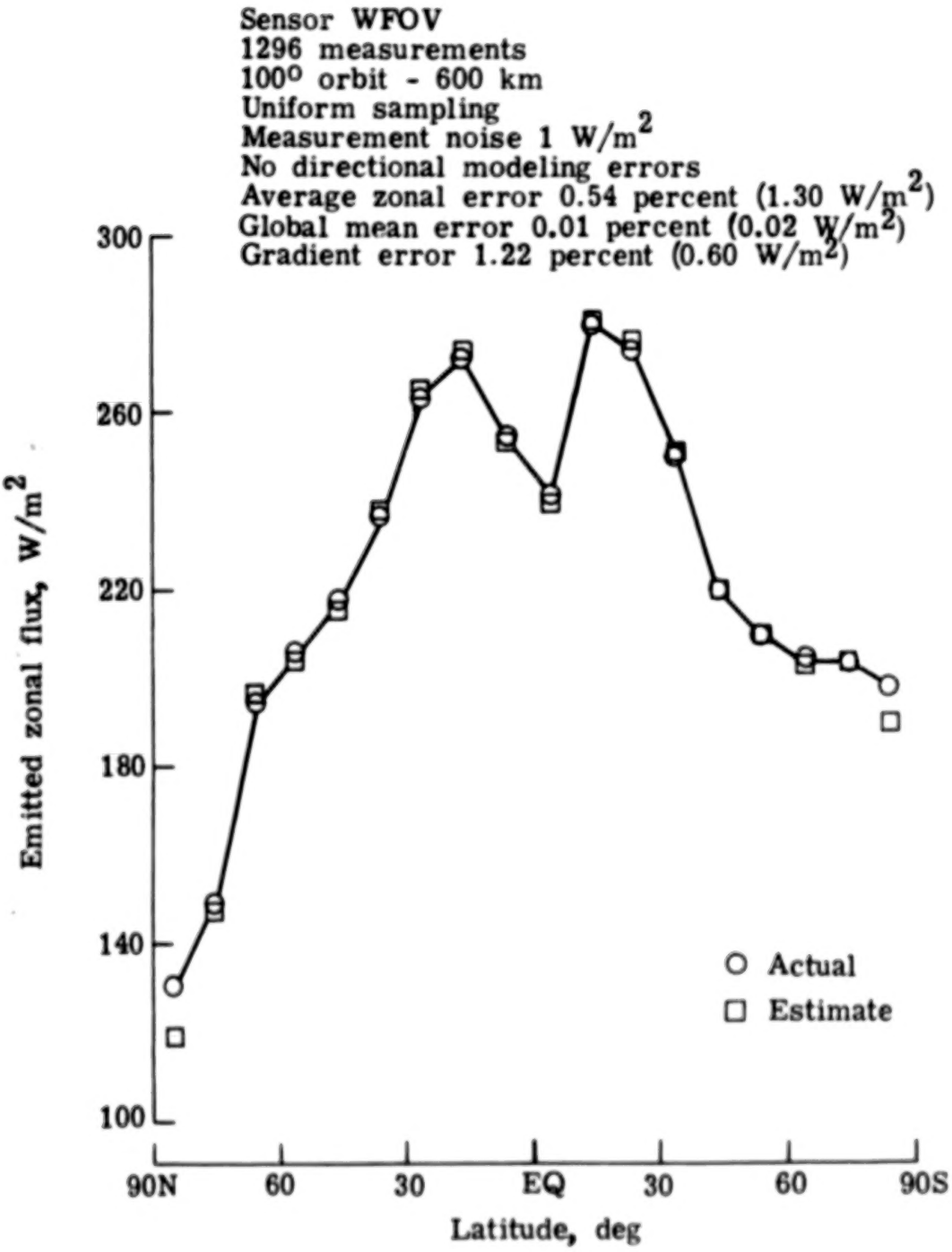

Figure 9.- WFOV estimates of average zonal emitted flux.

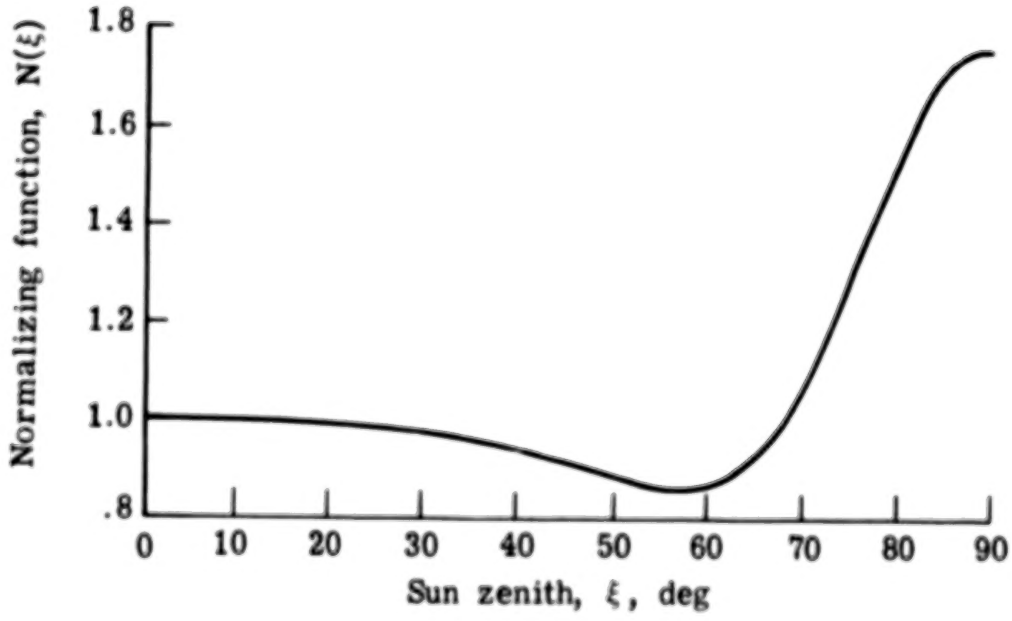

Figure 10.- Normalizing function for empirical bidirectional function.

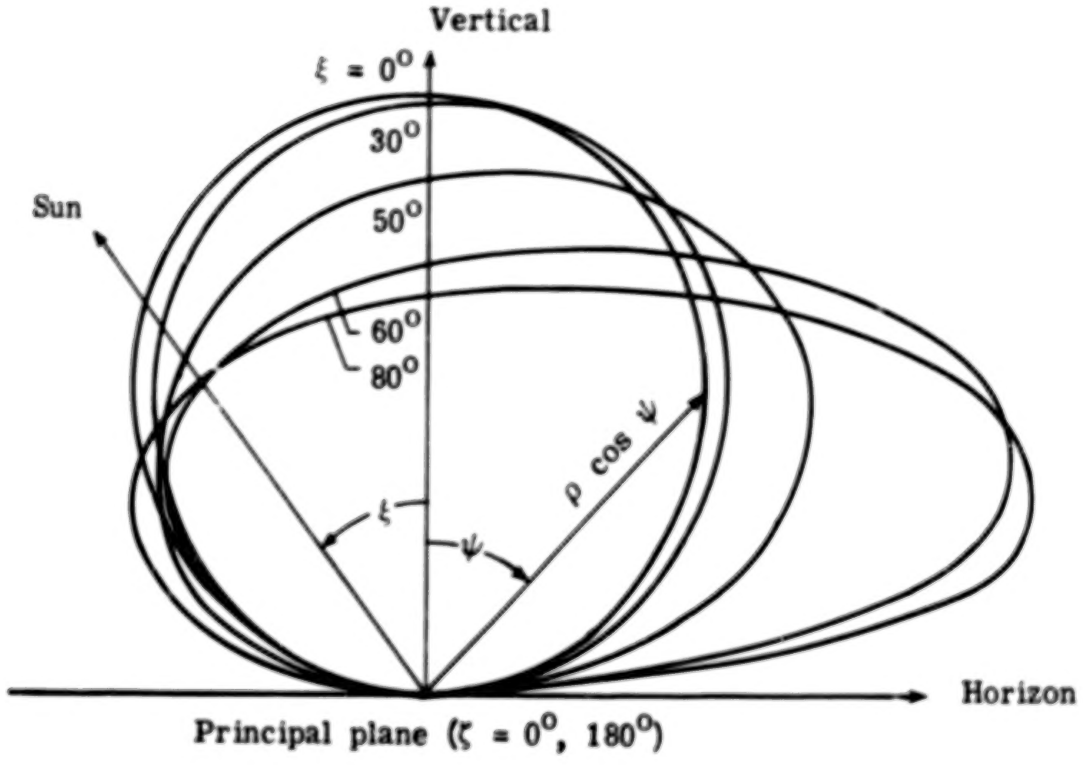

Principal plane ($\zeta = 0^\circ, 180^\circ$)

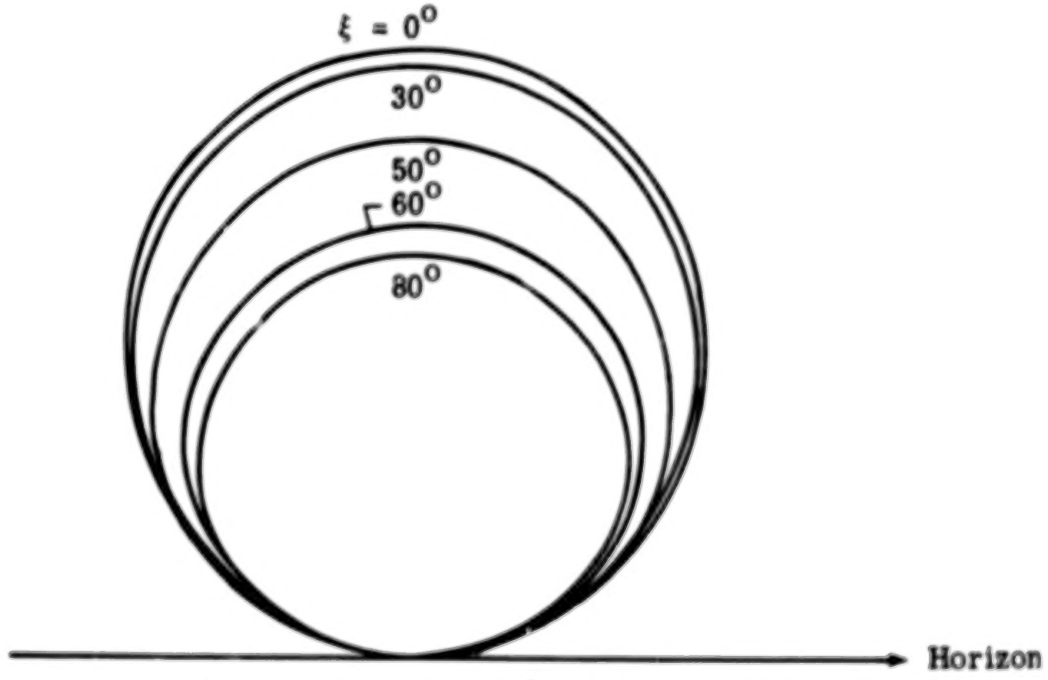

Normal plane ($\zeta = 90^\circ, 270^\circ$)

Figure 11.- An empirical bidirectional function.

$$\rho \cos \psi = \frac{\text{Reflected flux per unit solid angle}}{\text{Total reflected flux}}.$$

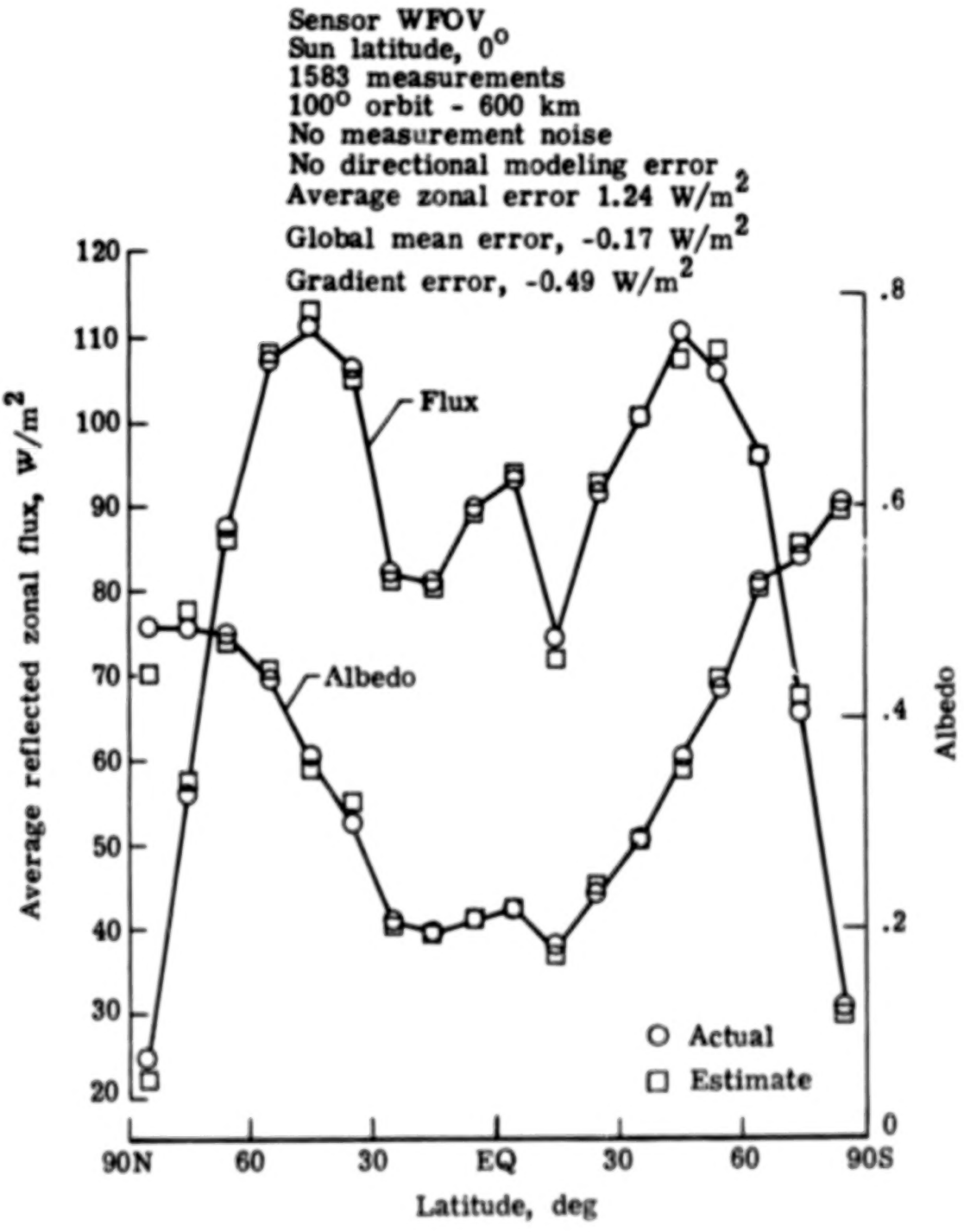

Figure 12.- WFOV estimates of average reflected zonal flux.

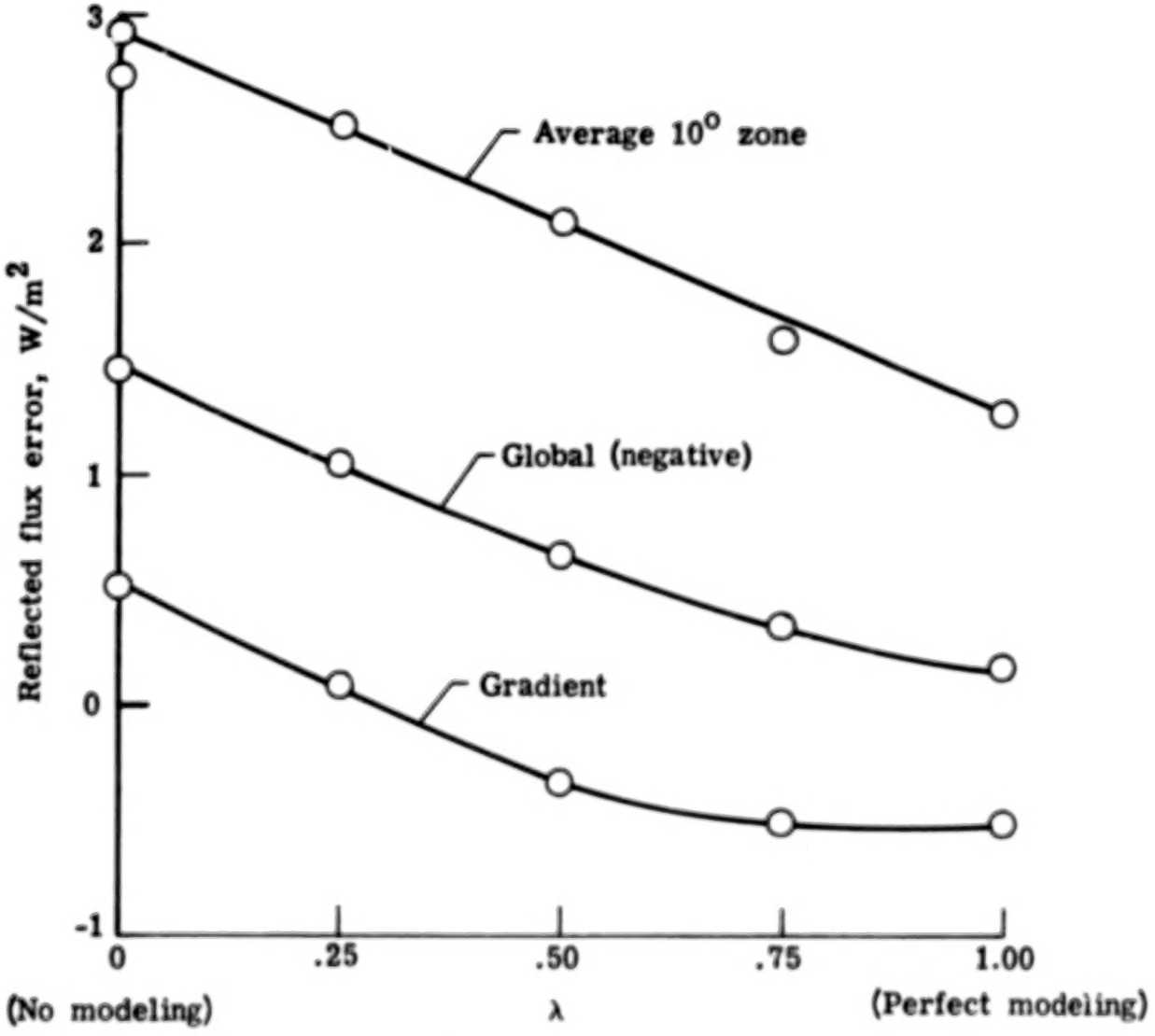

Figure 13.- Sensitivity of WFOV estimates to directional modeling errors. $i = 100^{\circ}$; $h = 600$ km; $J = 1600$; and $\sigma = 0$. $B = \lambda\rho - (1 - \lambda)\frac{1}{\pi}$.

Symbol	Sun longitude, deg	Number of measurements	Average zonal error, W/m^2	Global mean error, W/m^2	Gradient error, W/m^2
———	0	1600	1.24	-0.17	-0.49
- - - -	45	1700	1.23	-.08	-.74

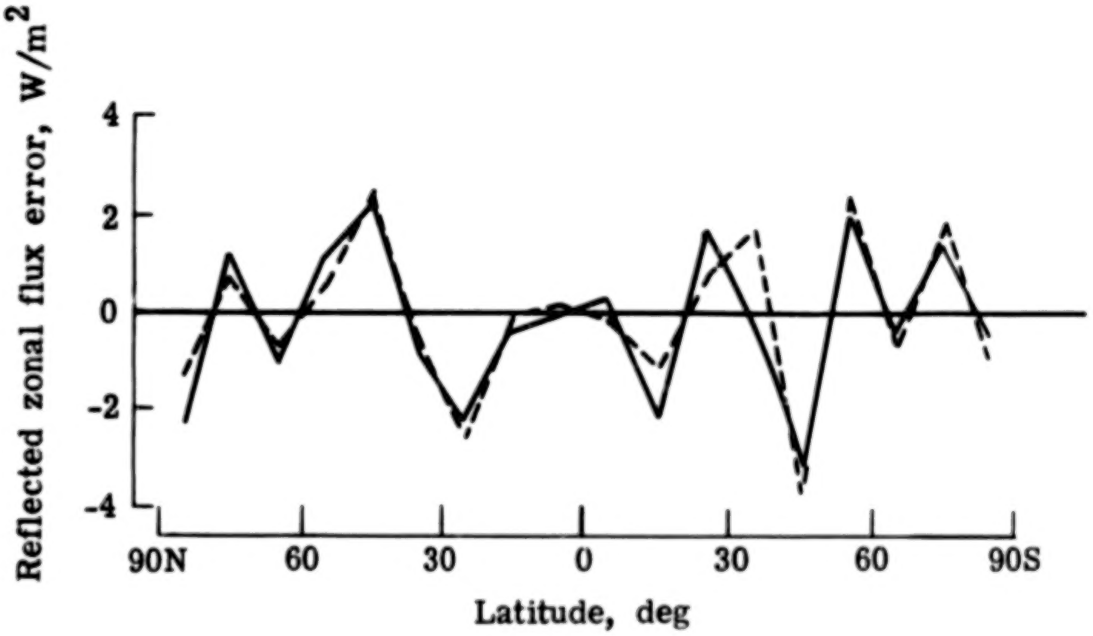

Figure 14.- Effect of sun longitude on WFOV estimates of reflected flux. $i = 100^o$; $h = 600$ km; $\lambda = 1$; and sun latitude, 0^o.

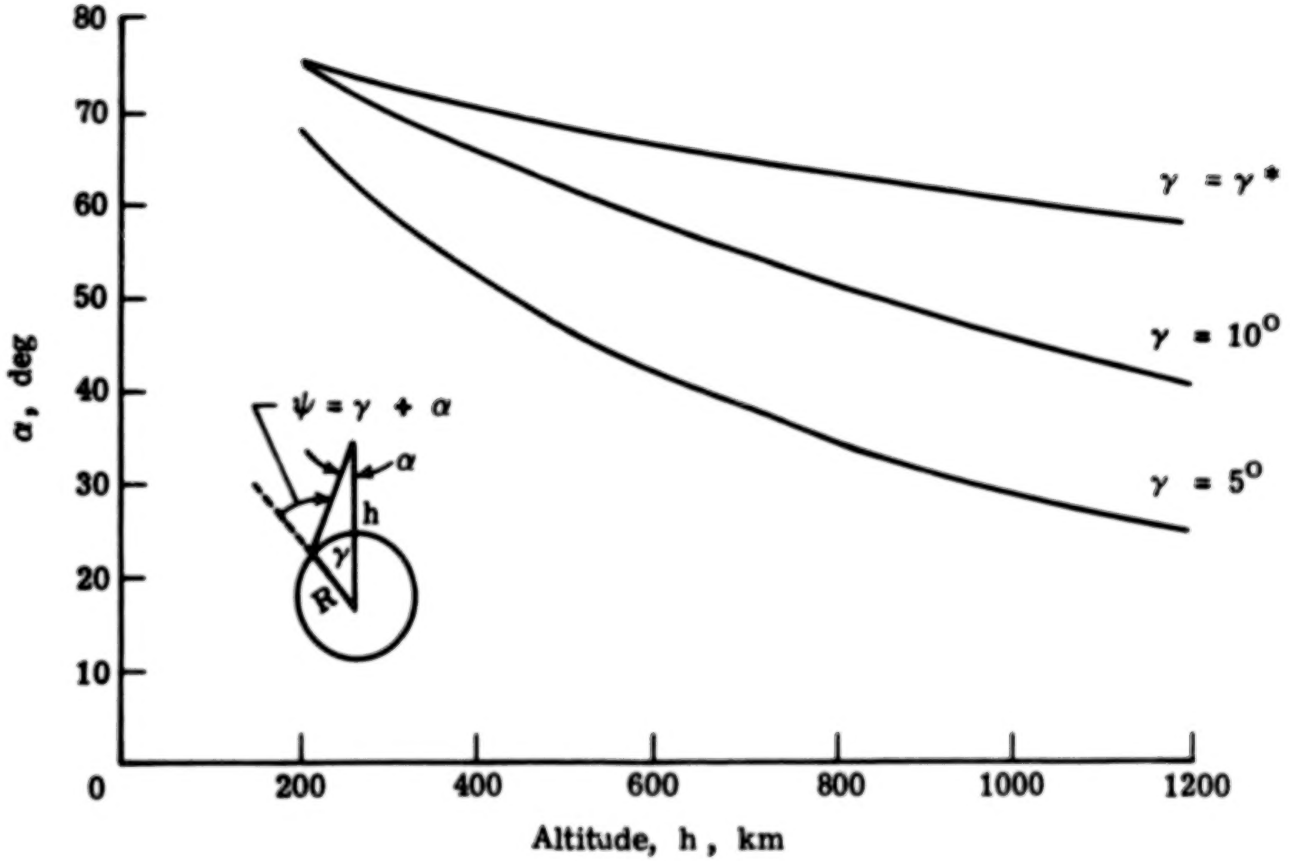

Figure 15.- Geometry of medium field of view sensor.

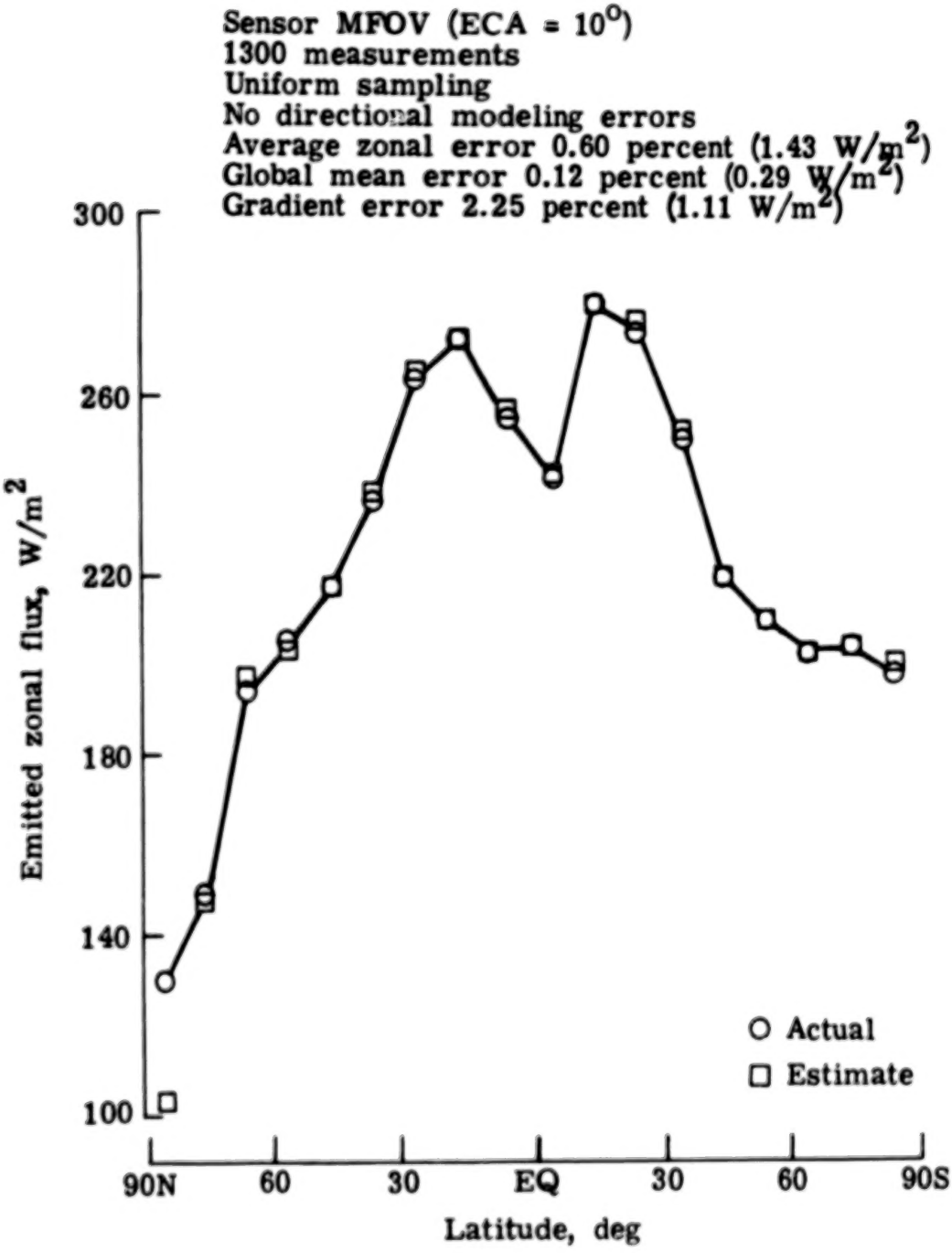

Figure 16.- MFOV estimates of average zonal emitted flux. $i = 100^{\circ}$; $h = 600$ km; $\sigma = 1$ W/m^2; and sun latitude, 0°.

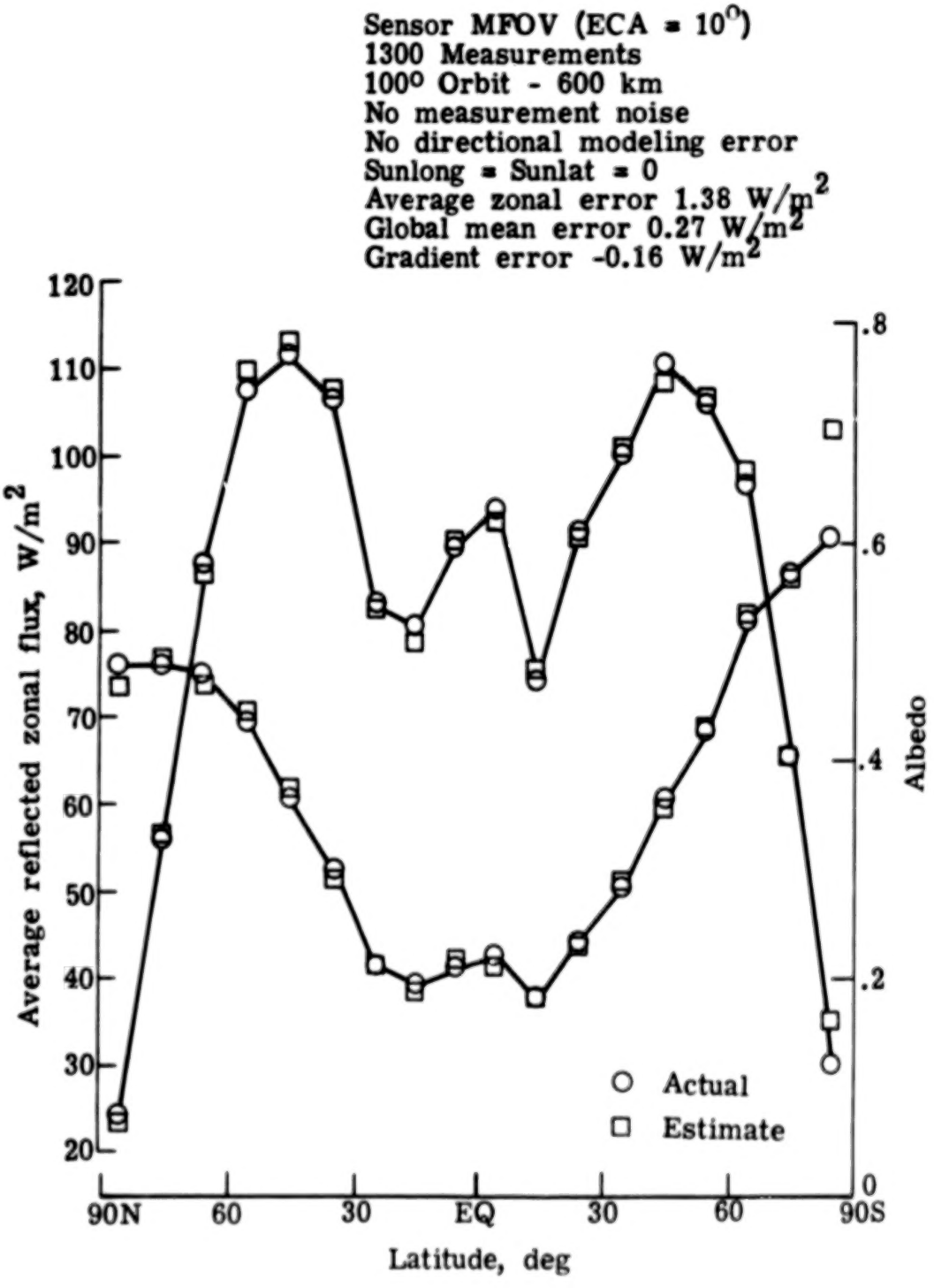

Figure 17.- MFOV estimates of average reflected zonal flux.

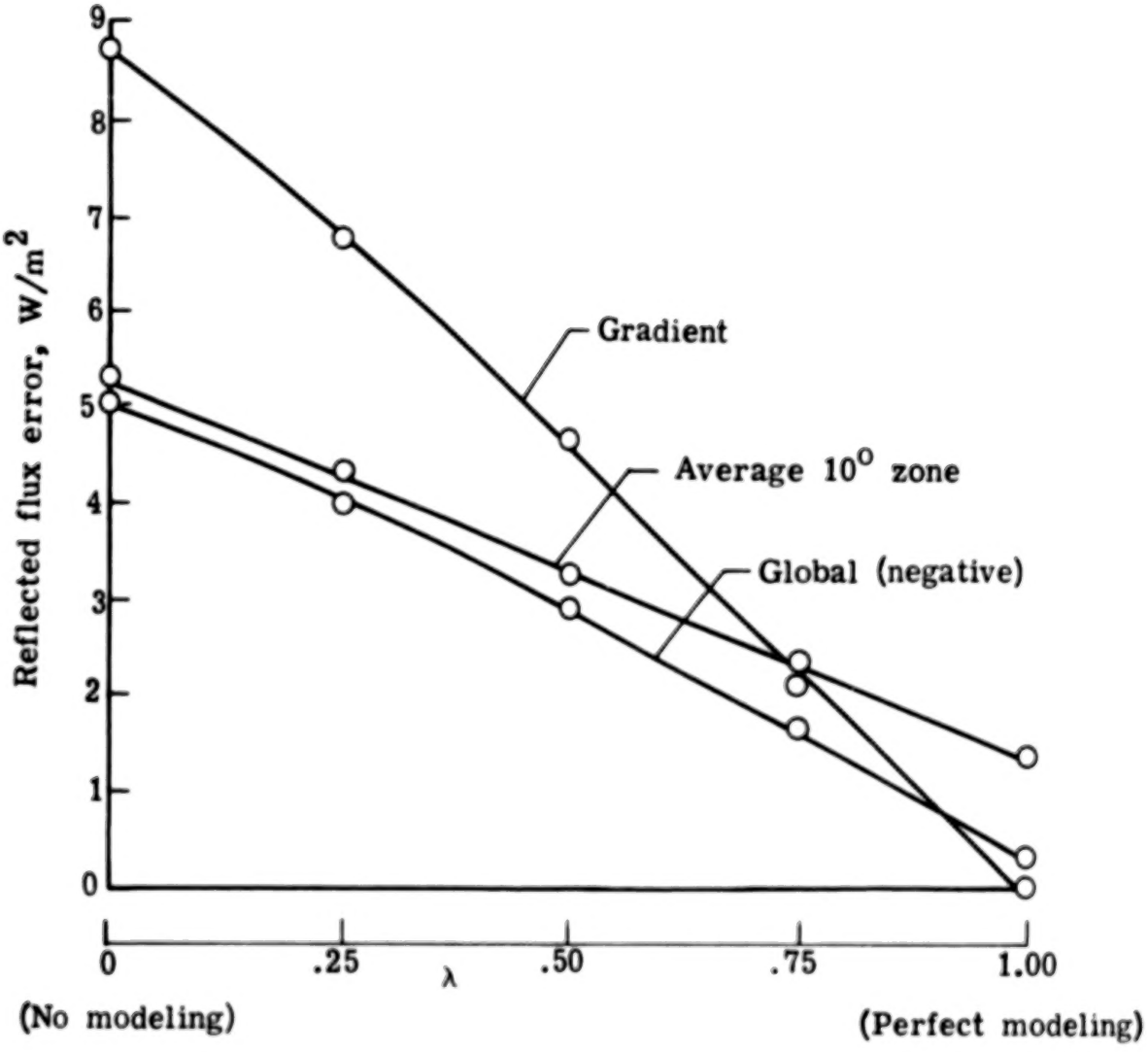

Figure 18.- Sensitivity of MPOV estimates to directional modeling errors. $i = 100^o$; $h = 600$ km; $ECA = 10^o$; $J = 1300$; and $\sigma = 0$. $B = \lambda\rho - (1 - \lambda)\frac{1}{\pi}$.

1. Report No.	2. Government Accession No.	3. Recipient's Catalog No.
NASA TP-1182		

4. Title and Subtitle	5. Report Date
SIMULATION STUDIES OF WIDE AND MEDIUM FIELD OF VIEW EARTH RADIATION DATA ANALYSIS	May 1978
	6. Performing Organization Code
7. Author(s)	8. Performing Organization Report No.
Richard N. Green	L-12003
	10. Work Unit No. 175-40-30-01
9. Performing Organization Name and Address	11. Contract or Grant No.
NASA Langley Research Center Hampton, VA 23665	
	13. Type of Report and Period Covered
12. Sponsoring Agency Name and Address	Technical Paper
National Aeronautics and Space Administration Washington, DC 20546	14. Sponsoring Agency Code

15. Supplementary Notes

16. Abstract

A parameter estimation technique is presented to estimate the radiative flux distribution over the Earth from radiometer measurements at satellite altitude. The technique analyzes measurements from a wide field of view (WFOV), horizon to horizon, nadir pointing sensor with a mathematical technique to derive the radiative flux estimates at the top of the atmosphere for resolution elements smaller than the sensor field of view. A computer simulation of the data analysis technique is presented for both Earth-emitted and reflected radiation. Zonal resolutions are considered as well as the global integration of plane flux. An estimate of the equator-to-pole gradient is obtained from the zonal estimates. Sensitivity studies of the derived flux distribution to directional model errors are also presented. In addition to the WFOV results, medium field of view results are presented.

17. Key Words (Suggested by Author(s))	18. Distribution Statement
Earth radiation Data analysis Simulation Earth radiation budget Orbital mechanics	Unclassified - Unlimited Subject Category 47

19. Security Classif. (of this report)	20. Security Classif. (of this page)	21. No. of Pages	22. Price*
Unclassified	Unclassified	45	$4.50

* For sale by the National Technical Information Service, Springfield, Virginia 22161

NASA-Langley, 1978